Computers and Structures 256 (2021) 106636

Contents lists available at ScienceDirect

Computers and Structures

journal homepage: www.elsevier.com/locate/compstruc

An isogeometric finite element-boundary element approach for the vibration analysis of submerged thin-walled structures

Alvaro del Toro Llorens [a,*], Josef Kiendl [a,b]

[a] Department of Marine Technology, Norwegian University of Science and Technology. Otto Nielsens veg 10, 7052 Trondheim, Norway
[b] Institute of Engineering Mechanics and Structural Analysis, Bundeswehr University Munich, Werner-Heisenberg-Weg 39, 85577 Neubiberg, Germany

ARTICLE INFO

Article history:
Received 1 September 2020
Accepted 7 July 2021
Available online 9 August 2021

Keywords:
Isogeometric analysis
Finite element method
Boundary element method
Modal analysis
Generalized added mass matrix

ABSTRACT

In this paper, the isogeometric formulations of the finite element and boundary element methods are applied to the dynamic analysis of thin-walled structures submerged in an infinite, inviscid, and incompressible fluid medium. This fluid–structure interaction problem is decoupled using the modal analysis technique, and the fluid effect on the structure is taken into account through the generalized added mass matrix. The structure is modeled with NURBS-based Kirchhoff–Love shell elements. The fluid response is computed using a regularized boundary integral equation. We take advantage of the geometry preserving property of the NURBS refinement techniques to reduce the computational cost without the need for a projection scheme. The implementation is benchmarked with three test cases, and good accuracy is obtained for a relatively low number of degrees of freedom.

1. Introduction

The prediction of the dynamic characteristics of structures immersed in a fluid of infinite extent is of relevant importance across multiple engineering disciplines, and one of the practical applications of structural acoustics. Accurate estimates of the wet natural frequencies and vibration modes are needed for a correct assessment of the dynamic response of, for instance, propellers, appendices, and submersibles in naval engineering or submerged floating tunnels in civil engineering.

There exist several numerical techniques and modeling considerations to tackle this fluid–structure interaction (FSI) problem. In general, the fluid is modeled as an inviscid acoustic medium, and whether or not its compressibility is included in the analysis depends on the frequency range of interest. In the low-frequency range, the fluid medium can be considered incompressible, it is governed by the Laplace's equation, and the effect of the fluid on the structure is embodied in an added-mass matrix [1]. In the high-frequency range, the fluid acts as a compressible medium, and its governing equation is the Helmholtz's equation.

Among the different numerical techniques available to the practitioner for solving this FSI problem, the most common ones are using the standard finite element method (FEM) for the structure, and for the fluid either a low order boundary element method (BEM) or the standard FEM as well. For the pros and cons of each combination of methods, an in-depth review can be found in [2]. Regardless of the numerical method, this FSI problem can be solved in a fully coupled manner [3–6], or it can be decoupled through the modal analysis approach [7–13] under the assumption that the structure preserves its *in-vacuo* eigenmodes when in contact with an incompressible fluid.

In the last 50 years, these methods have been successfully applied in the field of numerical structural acoustics since the pioneering work of Zienkiewicz and Newton [3] in 1969. They used a finite element-finite element approach to study the vibrations of submerged structures in a compressible fluid. Antoniadis and Kanarachos [7] proposed a decoupling procedure based on the modal superposition methodology for the eigenproblem of structures in contact with incompressible fluids. This latter procedure has been widely adopted in the literature for the free vibration analysis of submerged structures, i.e. partially liquid-filled cylinders [8], cantilever plates [9], and a container ship hull [11].

In these analyses there are two mesh generations involved, and in case each domain is meshed with a different mesh topology and/or density, a projection scheme between them is needed. This workflow can largely benefit from the adoption of the isogeometric analysis (IGA) framework [14], especially when only a surface representation of the body suffices for both the structural and fluid analyses. With IGA, the solution spaces inherit the basis functions used to describe the geometry, which is exactly represented in each domain and remains invariant to the refinement of the

* Corresponding author.
E-mail address: alvaro.deltoro@ntnu.no (A. del Toro Llorens).

https://doi.org/10.1016/j.compstruc.2021.106636
0045-7949/

solution spaces. The isogeometric formulation of the FEM and the BEM for structural dynamics and potential flow problems, respectively, has been proved to be superior to their standard formulations as reported in [15–17]. Furthermore, it has been recently applied to the hydroelastic analysis of partially submerged plates [12] and partially filled cylinders [13].

This work focuses on the application of the isogeometric formulation of the FEM and the BEM to the analysis of the natural frequencies of thin-walled structures submerged in a medium of infinite extent. These analyses fall in the low-frequency regime. Thus, the fluid is treated as an incompressible non-dissipative medium and the decoupled approach [7] is implemented. We use Non-Uniform Rational B-Splines (NURBS) surfaces to represent the geometry of the structures. The structural analysis is linear and is performed with NURBS-based Kirchhoff–Love shell finite elements [18], and the structural damping is neglected when computing the vibration modes.

The rest of this paper is organized as follows: Section 2 briefly introduces non-uniform rational B-splines surfaces; Section 3 presents the structural model based on the Kirchhoff–Love shell theory, the modal superposition approach, and how the geometric continuity of the deformed configuration can be enforced in geometries with poles; Section 4 details the formulation and implementation of the boundary element method within the isogeometric framework; Section 5 explains how we perform the modal analysis of a submerged structure; Section 6 contains three numerical examples validating the current numerical scheme; and finally Section 7 closes the document with the conclusions.

2. Non-Uniform Rational B-Splines

Non-Uniform Rational B-Splines are still the *de facto* standard for parametric surface representation within the CAD industry. NURBS have a high level of maturity in the CAD community, of flexibility for free-form modeling, and the ability to exactly represent all the conic sections. Consequently, the use of NURBS as basis functions becomes a natural choice in the isogeometric analysis framework.

A NURBS surface is a bivariate vector-valued piecewise rational function [19, p. 128] of the form

$$\mathbf{S}(\xi,\eta)=\sum_{i=1}^{n}\sum_{j=1}^{m}R_{i,j}(\xi,\eta)\mathbf{P}_{i,j} \tag{1}$$

where $\mathbf{P}_{i,j}\in\mathbb{R}^3$ defines a bidirectional net of control points; and $R_{i,j}(\xi,\eta)$ are the piecewise rational basis functions. These are defined as

$$R_{i,j}(\xi,\eta)=\frac{N_{i,p}(\xi)N_{j,q}(\eta)w_{i,j}}{\sum_{k=1}^{n}\sum_{l=1}^{m}N_{k,p}(\xi)N_{l,q}(\eta)w_{k,l}} \tag{2}$$

upon the non-rational B-spline basis functions $N_{i,p}(\xi), N_{j,q}(\eta)$; the degrees p and q in the parametric directions ξ and η, respectively; and the weights $w_{i,j}$ of the control points.

The B-spline basis functions are defined on the open knot vectors U and V, which are a non-decreasing and non-uniform sequence of real numbers,

$$U=\left[\underbrace{0,\dots,0}_{p+1},\xi_{p+2},\dots,\xi_n,\underbrace{1,\dots,1}_{p+1}\right] \tag{3}$$

$$V=\left[\underbrace{0,\dots,0}_{q+1},\eta_{q+2},\dots,\eta_m,\underbrace{1,\dots,1}_{q+1}\right] \tag{4}$$

and are evaluated with the Cox deBoor recurrence formula [20]:

$$p=0$$

$$N_{i,0}(\xi)=\begin{cases}1 & \xi_i\leqslant\xi<\xi_{i+1}\\ 0 & \text{otherwise}\end{cases} \tag{5}$$

$$p\geqslant 1$$

$$N_{i,p}(\xi)=\frac{\xi-\xi_i}{\xi_{i+p}-\xi_i}N_{i,p-1}(\xi)+\frac{\xi_{i+p+1}-\xi}{\xi_{i+p+1}-\xi_{i+1}}N_{i+1,p-1}(\xi) \tag{6}$$

3. Structural model

In this work, we use the Kirchhoff–Love shell theory to model thin-walled structures. Its isogeometric formulation for linear elasticity is briefly reviewed here. For a thorough elaboration, see [18,21].

In this section, geometric variables indicated with $(\mathring{\cdot})$ refer to the reference configuration. Greek indices take on values $\{1,2\}$, while Latin indices take on values $\{1,2,3\}$, and the Einstein summation convention is applied on repeated indices. The shell differential geometry is formulated in a convective curvilinear coordinate system $(\theta_1,\theta_2,\theta_3)$. The in-plane coordinates are denoted by θ_α and $\theta_3\in[-0.5h,0.5h]$ is the thickness coordinate, h being the shell thickness. Partial derivatives with respect to θ_α are indicated as $\partial(\cdot)_{,\alpha}=\partial(\cdot)/\partial\theta_\alpha$.

3.1. Shell differential geometry

By virtue of the Kirchhoff hypothesis (cross sections remain straight and orthogonal to the shell midsurface after deformation), the shell continuum can be described by the midsurface and its normal vector field. The position vector in the current configuration of an arbitrary material point of the shell continuum is defined as

$$\mathbf{x}(\theta_1,\theta_2,\theta_3)=\mathbf{r}(\theta_1,\theta_2)+\theta_3\,\mathbf{a}_3(\theta_1,\theta_2) \tag{7}$$

where $\mathbf{r}$ and $\mathbf{a}_3$ are, respectively, the position vector and the director or normal vector of a point on the midsurface ($\theta_3=0$). In the sequel, the explicit dependence of the geometric variables on θ_i is omitted to make the equations more compact.

Given a point $\mathbf{r}$ on the midsurface, the tangent base vectors of the midsurface are obtained by $\mathbf{a}_\alpha=\mathbf{r}_{,\alpha}$, and the director vector is computed as

$$\mathbf{a}_3=\frac{\mathbf{a}_1\times\mathbf{a}_2}{\|\mathbf{a}_1\times\mathbf{a}_2\|} \tag{8}$$

The covariant base vectors at a point in the shell continuum are denoted by $\mathbf{g}_i=\partial\mathbf{x}/\partial\theta_i$, and can be expressed in terms of the tangent base vectors of the midsurface $\mathbf{a}_i$ as follows:

$$\mathbf{g}_\alpha=\mathbf{a}_\alpha+\theta_3\mathbf{a}_{3,\alpha} \tag{9}$$

$$\mathbf{g}_3=\mathbf{a}_3 \tag{10}$$

The covariant metric coefficients denoted by $g_{ij}=\mathbf{g}_i\cdot\mathbf{g}_j$ are then computed as:

$$g_{\alpha\beta}=\mathbf{a}_\alpha\cdot\mathbf{a}_\beta+2\theta_3\mathbf{a}_{3,\alpha}\cdot\mathbf{a}_\beta+(\theta_3)^2\mathbf{a}_{3,\alpha}\cdot\mathbf{a}_{3,\beta} \tag{11}$$

$$g_{\alpha3}=\mathbf{a}_\alpha\cdot\mathbf{a}_3+\theta_3\mathbf{a}_{3,\alpha}\cdot\mathbf{a}_3=0 \tag{12}$$

$$g_{3\alpha}=\mathbf{a}_3\cdot\mathbf{a}_\alpha+\theta_3\mathbf{a}_3\cdot\mathbf{a}_{3,\alpha}=0 \tag{13}$$

$$g_{33}=\mathbf{a}_3\cdot\mathbf{a}_3=1 \tag{14}$$

Under the assumption of linear strain distribution through the thickness, the quadratic term in Eq. 11 can be neglected:

$$g_{\alpha\beta}=\mathbf{a}_\alpha\cdot\mathbf{a}_\beta+2\theta_3\mathbf{a}_{3,\alpha}\cdot\mathbf{a}_\beta \tag{15}$$

The contravariant metric coefficients denoted by g^{ij} are obtained from g_{ij} as follows:

$$[g^{\alpha\beta}] = [g_{\alpha\beta}]^{-1} \tag{16}$$
$$g^{\alpha 3} = 0 \tag{17}$$
$$g^{3\alpha} = 0 \tag{18}$$
$$g^{33} = 1 \tag{19}$$

where Eq. 16 has to be understood in matrix form. The contravariant base vectors denoted by $\mathbf{g}^i$ can be computed from the covariant base vectors, such that they satisfy the Kronecker delta property $\mathbf{g}^i \cdot \mathbf{g}_j = \delta^i_j$, and the contravariant metric coefficients:

$$\mathbf{g}^\alpha = g^{\alpha\beta}\mathbf{g}_\beta \tag{20}$$
$$\mathbf{g}^3 = \mathbf{g}_3 \tag{21}$$

Finally, Eqs. (7)–(21) hold analogously for the reference configuration ($\mathring{\mathbf{x}}$, $\mathring{\mathbf{r}}$, $\mathring{\mathbf{a}}_i$, $\mathring{\mathbf{g}}_i$, $\mathring{g}_{ij}$, $\mathring{\mathbf{g}}^i$ and $\mathring{g}^{ij}$).

3.2. Shell kinematics

The displacement field $\mathbf{v}$ of any point in the shell continuum is computed as the difference in the position vectors between the current and the reference configurations, leading to

$$\mathbf{v} = \mathbf{x} - \mathring{\mathbf{x}} = \mathbf{r} - \mathring{\mathbf{r}} + \theta_3\left(\mathbf{a}_3 - \mathring{\mathbf{a}}_3\right) = \mathbf{u} + \theta_3\left(\mathbf{a}_3 - \mathring{\mathbf{a}}_3\right) \tag{22}$$

where $\mathbf{u}$ is the displacement field of the shell midsurface. The partial derivatives of $\mathbf{v}$ with respect to $\theta_i$are

$$\mathbf{v}_{,\alpha} = \mathbf{u}_{,\alpha} + \theta_3\left(\mathbf{a}_{3,\alpha} - \mathring{\mathbf{a}}_{3,\alpha}\right) \tag{23}$$
$$\mathbf{v}_{,3} = \mathbf{a}_3 - \mathring{\mathbf{a}}_3 \tag{24}$$

As strain measure, we use the infinitesimal strain tensor, denoted as $\boldsymbol{\epsilon}$, and defined as the linearized Green - Lagrange strain tensor. This tensor is formulated in convective curvilinear coordinates as

$$\boldsymbol{\epsilon} = \epsilon_{ij}\,\mathring{\mathbf{g}}^i \otimes \mathring{\mathbf{g}}^j \tag{25}$$

with

$$\epsilon_{ij} = \frac{1}{2}\left(\mathbf{v}_{,i} \cdot \mathring{\mathbf{g}}_j + \mathbf{v}_{,j} \cdot \mathring{\mathbf{g}}_i\right) \tag{26}$$

In Kirchhoff–Love shells, transverse shear strains vanish, $\epsilon_{3\alpha} = 0$, while the transverse normal strain, $\epsilon_{33} \neq 0$, is statically condensed, and hence, only in-plane strain components $\epsilon_{\alpha\beta}$ are considered. Close inspection of the Eqs. 23, 24, and 26 reveals that, after neglecting quadratic terms of θ_3, the in-plane strains are the sum of a constant term representing membrane strains and a linear term representing bending strains:

$$\epsilon_{\alpha\beta} = \epsilon^m_{\alpha\beta} + \theta_3\kappa_{\alpha\beta} \tag{27}$$

where the membrane strains are denoted by $\epsilon^m_{\alpha\beta}$, while $\kappa_{\alpha\beta}$ corresponds to the change in curvature, and therefore $\theta_3\,\kappa_{\alpha\beta}$ represents the bending strains. The linear equations of these strain contributions are:

$$\epsilon^m_{\alpha\beta} = \frac{1}{2}\left(\mathbf{u}_{,\alpha} \cdot \mathring{\mathbf{a}}_\beta + \mathbf{u}_{,\beta} \cdot \mathring{\mathbf{a}}_\alpha\right) \tag{28}$$

$$\kappa_{\alpha\beta} = -\mathring{\mathbf{a}}_3 \cdot \mathbf{u}_{,\alpha\beta} + \frac{1}{\|\mathring{\mathbf{a}}_1 \times \mathring{\mathbf{a}}_2\|}\left[\left(\mathring{\mathbf{r}}_{,\alpha\beta} \times \mathring{\mathbf{a}}_2\right) \cdot \mathbf{u}_{,1} + \left(\mathring{\mathbf{a}}_1 \times \mathring{\mathbf{r}}_{,\alpha\beta}\right) \cdot \mathbf{u}_{,2} + \mathring{\mathbf{r}}_{,\alpha\beta} \cdot \mathring{\mathbf{a}}_3\left(\left(\mathring{\mathbf{a}}_2 \times \mathring{\mathbf{a}}_3\right) \cdot \mathbf{u}_{,1} + \left(\mathring{\mathbf{a}}_3 \times \mathring{\mathbf{a}}_1\right) \cdot \mathbf{u}_{,2}\right)\right] \tag{29}$$

Eq. 28 and Eq. 29 show that this shell formulation is rotation-free because the kinematics of the shell is described by the three components of the displacement field of the shell midsurface. Therefore, this is the field to be solved for.

3.3. Constitutive equation

In this study, a linear elastic, isotropic material model is used. The constitutive equation is formulated in terms of the Cauchy stress tensor $\boldsymbol{\sigma}$, the linearized Green - Lagrange strain tensor $\boldsymbol{\epsilon}$, and the elasticity tensor $\mathbb{C}$:

$$\boldsymbol{\sigma} = \mathbb{C} : \boldsymbol{\epsilon} \tag{30}$$

For an isotropic material, the components of $\mathbb{C}$ defined in the convective curvilinear coordinate system are given by

$$\mathbb{C}_{ijkl} = \lambda\left(\mathring{g}^{ij}\,\mathring{g}^{kl}\right) + \mu\left(\mathring{g}^{ik}\,\mathring{g}^{jl} + \mathring{g}^{il}\,\mathring{g}^{jk}\right) \tag{31}$$

where λ and μ are the Lamé constants. They are expressed in terms of the Young's modulus E and the Poisson's ratio ν as

$$\lambda = \frac{\nu E}{(1+\nu)(1-2\nu)} \tag{32}$$
$$\mu = \frac{E}{2(1+\nu)} \tag{33}$$

Enforcing the plane stress condition ($\sigma_{33} = 0$) allows eliminating the transverse normal strain ϵ_{33} by static condensation of the material tensor:

$$\sigma_{33} = \mathbb{C}_{33\alpha\beta}\epsilon_{\alpha\beta} + \mathbb{C}_{3333}\epsilon_{33} = 0 \tag{34}$$

Implying that:

$$\epsilon_{33} = -\frac{\mathbb{C}_{33\alpha\beta}}{\mathbb{C}_{3333}}\epsilon_{\alpha\beta} \tag{35}$$

In addition, in the Kirchhoff–Love shell theory the transverse shear deformations are neglected. Then, the equations involving the shear stresses and strains are removed from Eq. 30. Based on this and Eq. 35, the constitutive equation becomes

$$\sigma_{\alpha\beta} = \left(\mathbb{C}_{\alpha\beta\gamma\delta} - \frac{\mathbb{C}_{\alpha\beta 33}\mathbb{C}_{33\gamma\delta}}{\mathbb{C}_{3333}}\right)\epsilon_{\gamma\delta} = \hat{\mathbb{C}}_{\alpha\beta\gamma\delta}\,\epsilon_{\gamma\delta} \tag{36}$$

where $\hat{\mathbb{C}}_{\alpha\beta\gamma\delta}$ is the statically condensed material tensor.

3.4. Variational formulation

The variational formulation is based on the principle of virtual work:

$$\delta W = \delta W^{int} - \delta W^{ext} + \delta W^{kin} = 0 \tag{37}$$

where δW is the virtual total work; δW^{int} is the virtual internal work; δW^{ext} is the virtual external work; δW^{kin} is the virtual inertial work; and $\delta(\cdot)$ denotes the variation of a quantity $(\cdot)$ with respect to a virtual displacement.

The virtual internal work takes the form

$$\delta W^{int} = \int_V (\delta\boldsymbol{\epsilon} : \boldsymbol{\sigma})\mathrm{d}V \tag{38}$$

where V is the volume of the structural domain and $\delta\boldsymbol{\epsilon}$ is the virtual strain. Eq. 38 is the general formula for the virtual internal work in linear elasticity, but we are interested in its particular form for shells with a linear stress–strain relation. Introducing Eq. 27 and Eq. 36 in tensor form into Eq. 38, δW^{int} reads as

$$\delta W^{int} = \int_V \left(\delta\boldsymbol{\epsilon}^m : \hat{\mathbb{C}} : \boldsymbol{\epsilon}^m + \delta\boldsymbol{\epsilon}^m : \hat{\mathbb{C}} : \theta_3\boldsymbol{\kappa} + \theta_3\delta\boldsymbol{\kappa} : \hat{\mathbb{C}} : \boldsymbol{\epsilon}^m + \theta_3\delta\boldsymbol{\kappa} : \hat{\mathbb{C}} : \theta_3\boldsymbol{\kappa}\right)\mathrm{d}V \tag{39}$$

with $\delta\boldsymbol{\epsilon}^m$ and $\delta\boldsymbol{\kappa}$ being, respectively, the virtual membrane strain and the virtual change in curvature.

Integrating through the thickness in Eq. 39, the second and third terms vanish because, when the material is homogeneous, they correspond to the integration of an odd function over a symmetrical domain. Then, the virtual internal work for a Kirchhoff–Love shell with a linear stress–strain relation becomes

$$\delta W^{int} = \int_S (\delta \boldsymbol{\epsilon}^m : \mathbf{n} + \delta \boldsymbol{\kappa} : \mathbf{m}) \mathrm{d}S \tag{40}$$

where S is the shell midsurface, and $\mathbf{n}$ and $\mathbf{m}$ are the stress resultant tensors, respectively, for the normal forces and the bending moments, and whose formulas are

$$\mathbf{n} = \int_{-h/2}^{h/2} \left(\hat{\mathbb{C}} : \boldsymbol{\epsilon}^m\right) \mathrm{d}\theta_3 = h\left(\hat{\mathbb{C}} : \boldsymbol{\epsilon}^m\right) \tag{41}$$

$$\mathbf{m} = \int_{-h/2}^{h/2} \left(\hat{\mathbb{C}} : \boldsymbol{\kappa}\right) \theta_3^2 \mathrm{d}\theta_3 = \frac{h^3}{12}\left(\hat{\mathbb{C}} : \boldsymbol{\kappa}\right) \tag{42}$$

The virtual external and kinetic works for a shell can be formulated as

$$\delta W^{ext} = \int_S (\delta \mathbf{u} \cdot \mathbf{t}) \mathrm{d}S \tag{43}$$

$$\delta W^{kin} = \int_S (\delta \mathbf{u} \cdot \rho_s \ddot{\mathbf{u}}) h \mathrm{d}S \tag{44}$$

where $\mathbf{t}$ denotes the external load per unit area, ρ_s is the material density, $\ddot{\mathbf{u}}$ is the acceleration vector, and it has been assumed that the differential of volume $\mathrm{d}V$ can be approximated by $\mathrm{d}V \approx h\mathrm{d}S$ [22].

3.5. Discretization

The discretized displacement field of the shell midsurface is expressed as:

$$\mathbf{u}\left(\mathring{\mathbf{r}}, t\right) = \sum_{j=1}^{n} R_j\left(\mathring{\mathbf{r}}\right) \hat{\mathbf{u}}^j(t) \tag{45}$$

where t is the time variable, R_j are the shape functions, n is the total number of shape functions, and $\hat{\mathbf{u}}^j$are the nodal displacement vectors or control points of the displacement field with the components $\hat{u}_i^j (i = 1, 2, 3)$ referring to the global x-,y-,z-components. The global degree of freedom number r of a nodal displacement is defined by $r = 3(j-1) + i$, such that $\hat{u}_r = \hat{u}_i^j$. The variation of $\mathbf{u}$ with respect to $\hat{u}_r$ is obtained by the partial derivative $\partial/\partial\hat{u}_r$:

$$\frac{\partial \mathbf{u}}{\partial \hat{u}_r} = R_j \mathbf{e}_i \tag{46}$$

where $\mathbf{e}_i$ is the global Cartesian base vector.

The variations of δW^{int}, δW^{ext}, and δW^{kin} yield, respectively, the vectors of internal, external and kinetic forces, $\mathbf{f}^{int}$, $\mathbf{f}^{ext}$, and $\mathbf{f}^{kin}$, such that Eq. 37 becomes:

$$\mathbf{f}^{kin} + \mathbf{f}^{int} = \mathbf{f}^{ext} \tag{47}$$

with:

$$f_r^{kin} = \int_S \rho_s \left(\frac{\partial \mathbf{u}}{\partial \hat{u}_r} \cdot \ddot{\mathbf{u}}\right) h \mathrm{d}S \tag{48}$$

$$f_r^{int} = \int_S \left(\frac{\partial \boldsymbol{\epsilon}^m}{\partial \hat{u}_r} : \mathbf{n} + \frac{\partial \boldsymbol{\kappa}}{\partial \hat{u}_r} : \mathbf{m}\right) \mathrm{d}S \tag{49}$$

$$f_r^{ext} = \int_S \frac{\partial \mathbf{u}}{\partial \hat{u}_r} \cdot \mathbf{t} \mathrm{d}S \tag{50}$$

The derivative of the vector of kinetic forces with respect to an acceleration degree of freedom $\ddot{u}_s$ yields the global consistent mass matrix:

$$M_{rs} = \int_S \rho_s \left(\frac{\partial \mathbf{u}}{\partial \hat{u}_r} \cdot \frac{\partial \ddot{\mathbf{u}}}{\partial \ddot{u}_s}\right) h \mathrm{d}S = \int_S \rho_s \left(\frac{\partial \mathbf{u}}{\partial \hat{u}_r} \cdot \frac{\partial \mathbf{u}}{\partial \hat{u}_s}\right) h \mathrm{d}S \tag{51}$$

The components of the global stiffness matrix are computed from the derivative of the vector of internal forces with respect to $\hat{u}_s$:

$$K_{rs} = \int_S \left(\frac{\partial^2 \boldsymbol{\epsilon}^m}{\partial \hat{u}_s \partial \hat{u}_r} : \mathbf{n} + \frac{\partial \boldsymbol{\epsilon}^m}{\partial \hat{u}_r} : \frac{\partial \mathbf{n}}{\partial \hat{u}_s} + \frac{\partial^2 \boldsymbol{\kappa}}{\partial \hat{u}_s \partial \hat{u}_r} : \mathbf{m} + \frac{\partial \boldsymbol{\kappa}}{\partial \hat{u}_r} : \frac{\partial \mathbf{m}}{\partial \hat{u}_s}\right) \mathrm{d}S \tag{52}$$

For a geometrically linear analysis, there is no distinction between the current and the reference configurations. Since $\boldsymbol{\epsilon}^m$ and $\boldsymbol{\kappa}$ are computed as the difference of these quantities between these two configurations, they become zero, and also $\mathbf{n}$ and $\mathbf{m}$. Therefore, the linear stiffness matrix becomes:

$$K_{rs}^{linear} = \int_S \left(\frac{\partial \boldsymbol{\epsilon}^m}{\partial \hat{u}_r} : \frac{\partial \mathbf{n}}{\partial \hat{u}_s} + \frac{\partial \boldsymbol{\kappa}}{\partial \hat{u}_r} : \frac{\partial \mathbf{m}}{\partial \hat{u}_s}\right) \mathrm{d}S \tag{53}$$

3.6. Modal superposition and the generalized equation of motion

The discrete equilibrium equation derived from Eq. 37 and governing the linear elastodynamic response of a conservative system with arbitrary initial conditions is

$$\mathbf{M} \cdot \ddot{\hat{\mathbf{u}}} + \mathbf{K} \cdot \hat{\mathbf{u}} = \mathbf{f} \tag{54}$$

where $\mathbf{M}$ is the consistent structural mass matrix defined by Eq. 51; $\mathbf{K}$ is the structural stiffness matrix defined by Eq. 53; $\mathbf{f}$ is the consistent nodal vector of external loads acting on the structure defined by Eq. 50; $\hat{\mathbf{u}}$ is the vector of displacements; and dots indicate partial differentiation with respect to time.

The free response ($\mathbf{f} = \mathbf{0}$) of the undamped system is a harmonic motion, and the displacement vector can be expressed as

$$\hat{\mathbf{u}} = \boldsymbol{\psi} e^{i\omega t} \tag{55}$$

where $\boldsymbol{\psi}$ defines the vibration mode; ω is the angular frequency of the free vibration; and i is the unit imaginary number. Combining Eq. 55 and Eq. 54 for the free vibration case leads to the generalized eigenproblem

$$\mathbf{K} \cdot \boldsymbol{\psi} = \omega^2 \mathbf{M} \cdot \boldsymbol{\psi} \tag{56}$$

whose solutions are the *in-vacuo* natural frequencies and vibration modes.

These vibration modes define a basis of orthogonal vectors that serve to represent any displacement vector [23]. The latter can be computed as a superposition of the vibration modes, each of them scaled by a weight that changes over time. These weights are called generalized coordinates, modal coordinates, or normal coordinates [23]. Thus, the displacement vector is expressed as

$$\hat{\mathbf{u}}(t) = \sum_{k=1}^{m} \boldsymbol{\psi}_k z_k(t) \tag{57}$$

being m the total number of modes; $\boldsymbol{\psi}_k$ the kth-vibration mode; and

$$z_k(t) = z_k e^{i\omega_k t} \tag{58}$$

the kth-generalized coordinate.

Collecting column-wise the m vibration modes into a matrix, called the *in-vacuo* modal matrix $\boldsymbol{\Psi}$, and the generalized coordinates into a vector $\mathbf{z}$, Eq. 57 can be written in matrix form

$$\hat{\mathbf{u}}(t) = \boldsymbol{\Psi} \cdot \mathbf{z}(t) \tag{59}$$

Combining Eq. 59 with Eq. 54 and premultiplying the resulting equation by $\boldsymbol{\Psi}^T$, we arrive to the generalized equation of motion

$$\tilde{\mathbf{M}} \cdot \ddot{\mathbf{z}} + \tilde{\mathbf{K}} \cdot \mathbf{z} = \tilde{\mathbf{f}} \tag{60}$$

being $\widetilde{\mathbf{M}} = \boldsymbol{\Psi}^T \cdot \mathbf{M} \cdot \boldsymbol{\Psi}$ the generalized consistent structural mass matrix; $\widetilde{\mathbf{K}} = \boldsymbol{\Psi}^T \cdot \mathbf{K} \cdot \boldsymbol{\Psi}$ the generalized structural stiffness matrix; and $\tilde{\mathbf{f}} = \boldsymbol{\Psi}^T \cdot \mathbf{f}$ the generalized external force vector.

3.7. A master–slave approach to enforce the G^1 continuity

The NURBS-based Kirchhoff–Love shell theory requires that the NURBS patches modeling a structure have at least G^1 continuity. Even though in this work the geometries are single-patch smooth NURBS surfaces, they contain C^0 knot lines. These lines act as hinge lines when the structure deforms, and hence they will turn into G^0 lines if the G^1 continuity is not enforced.

The enforcement of this condition can be achieved through different techniques. For instance, with the bending strip method [24], the penalty method [25–27], the Lagrange multipliers method [28], or the master–slave approach [18], among others. In this work, we opt for the master–slave approach because of being a simple yet effective method for the problems at hand.

The geometries that we use for the benchmark examples in Section 6 are single-patch closed surfaces of revolution. Due to how they are constructed, they contain three C^0 knot lines along the direction of revolution, and in the particular case of the sphere, also one in the circumferential direction. Additionally, at the poles and along the edges closing the surface, not only the G^1 continuity must be enforced but also the G^0 continuity to ensure that the surface remains watertight for any deformed configuration.

Owing to the trivial character of the linear constraint to enforce the G^0 continuity, only the linear constraints to impose the G^1 continuity are presented hereafter. Let k be the row (column) number of the polygon of control points aligned with a C^0 knot line. The geometry is G^1 continuous if across this line the following relation holds in homogeneous coordinates [18,21]

$$\left(\mathbf{P}^w_{k+1,j} - \mathbf{P}^w_{k,j}\right) = c_j \left(\mathbf{P}^w_{k,j} - \mathbf{P}^w_{k-1,j}\right) \tag{61}$$

where c_j is the scalar coefficient corresponding to the jth-column (row) of control points and is computed as follows:

$$c_j = \frac{\|\mathbf{P}^w_{k+1,j} - \mathbf{P}^w_{k,j}\|}{\|\mathbf{P}^w_{k,j} - \mathbf{P}^w_{k-1,j}\|} \tag{62}$$

The geometrical interpretation of this condition is that these three control points must be collinear. Across this C^0 knot line, the deformed geometry will be G^1 continuous if the Eq. 61 also holds in the deformed configuration [21, p. 70], yielding the following constraint for the control points of the displacement field

$$\hat{\mathbf{u}}_{k+1,j} = (1 + c_j)\hat{\mathbf{u}}_{k,j} - c_j \hat{\mathbf{u}}_{k-1,j} \tag{63}$$

where $\hat{\mathbf{u}}_{k+1,j}$ is taken as the slave, and $\hat{\mathbf{u}}_{k,j}$ and $\hat{\mathbf{u}}_{k-1,j}$ as the masters.

The imposition of the G^1 continuity at a pole requires that the first and second, or the next-to-last and last, rows (columns) of control points are coplanar in the deformed configuration. To enforce this coplanarity with a master–slave approach, three of these control points must always act as master, and as many constraints as the remaining number of control points are required.

At the pole, only one control point acts as master since all the others are slaves of the former after imposing the G^0 continuity. At the row (column) of control points contiguous to the pole, only two of these control points can always act as master, and they cannot be collinear with the master control point at the pole. In this manner, these three master control points will define the tangent plane at the pole.

Fig. 1 illustrates the application of Eq. 63 to two cases that differ in the number of control points influencing the continuity at the pole. In this figure, the constraints between points are represented with colored rectangles, and m and s stand for master and slave, respectively. The color of these letters relates them to the constraint in which they are involved. This figure shows that depending on the number of points at the row (column) of control points contiguous to the pole, it can happen that Eq. 63 cannot be applied the required number of times. Consequently, at this row (column) the number of control points that are always master can be larger than two. Whereas in Fig. 1 (a) it is possible to build the required number of constraints, in Fig. 1 (b) only 12 out of 14 constraints can be established. Therefore, it is desirable an alternative approach that works for any number of control points. The way we achieve it is through the triangular or area coordinates [29, p. 173].

Let us assume that the pole is defined by the collapsed control points of the first row. We choose three control points as masters, $\mathbf{P}^{m_1}, \mathbf{P}^{m_2}$ and $\mathbf{P}^{m_3}$, one at the pole and the other two at the second row of control points with the sole condition that they are non-collinear. Then, we compute the area coordinates $\boldsymbol{\zeta} = (\zeta_1, \zeta_2, \zeta_3)$ for the remaining (slave) control points of the second row. In this work, the poles of the geometry are always on the Cartesian X axis, and the tangent planes at the poles in the undeformed configuration are parallel to the Cartesian YZ plane. Therefore, only the Y and Z Cartesian coordinates of the masters and slaves are used to compute the area coordinates.

Let $\hat{\mathbf{u}}^s$ be the displacement degrees of freedom of one of the slaves and $\boldsymbol{\zeta}^s$ its area coordinates, the linear constraint equation is

$$\hat{\mathbf{u}}^s = [\hat{\mathbf{u}}^{m_1}, \hat{\mathbf{u}}^{m_2}, \hat{\mathbf{u}}^{m_3}] \cdot \boldsymbol{\zeta}^s \tag{64}$$

where $\hat{\mathbf{u}}^{m_1}, \hat{\mathbf{u}}^{m_2}$ and $\hat{\mathbf{u}}^{m_3}$ are the degrees of freedom of the displacements of the master control points $\mathbf{P}^{m_1}, \mathbf{P}^{m_2}$ and $\mathbf{P}^{m_3}$, respectively. Fig. 2 illustrates an example of the application of these constraints with a static analysis where the coplanarity of the control points at the pole is highlighted in yellow.

4. Fluid model

4.1. Boundary value problem

We consider a 3D body with boundary Γ_b submerged in an inviscid, incompressible, and non-flowing fluid. The fluid domain Ω is of infinite extent. Assuming that the fluid motion will be irrotational, there exist a velocity potential $\Phi(\mathbf{x})$ such that its gradient is the fluid velocity $\nabla\Phi(\mathbf{x}) = \mathbf{v}(\mathbf{x})$. Furthermore, $\Phi(\mathbf{x})$ is the solution of the following boundary value problem (BVP):

$$\nabla^2\Phi = 0, \quad \forall \mathbf{x} \in \Omega \tag{65}$$

$$\frac{\partial\Phi}{\partial n} = \mathbf{v}_b \cdot \mathbf{n}, \quad \forall \mathbf{x} \in \Gamma_b \tag{66}$$

$$\Phi = 0, \quad \text{if} \quad \|\mathbf{x}\| \to \infty \tag{67}$$

where $\mathbf{v}_b$ is the body surface velocity and $\mathbf{n}$ is the unit outward normal vector pointing from the body surface into the fluid. In this BVP, Eq. 66 represents the impermeability boundary condition on the body surface, and Eq. 67 is the condition at infinity.

4.2. Boundary integral equation

Applying the Green's second identity [30,31] to $\Phi(\mathbf{x})$ and to the fundamental solution of the Laplace equation in 3D defined by $G(\mathbf{x}, \mathbf{y}) = -1/(4\pi r)$, with $r = \|\mathbf{x} - \mathbf{y}\|$, one can recast the BVP into a Fredholm boundary integral equation of the second kind with respect to $\Phi(\mathbf{x})$:

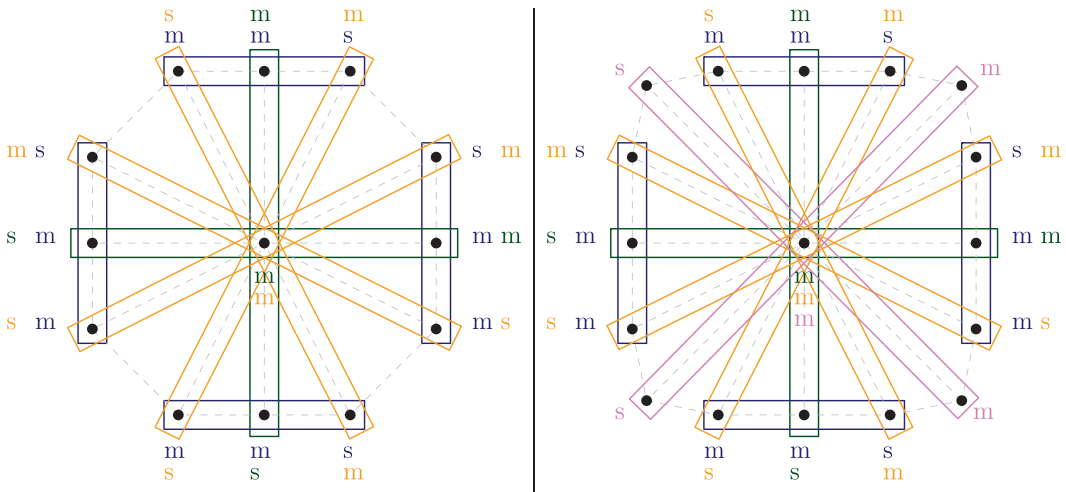

(a) Successful case. (b) Unsuccessful case.

Fig. 1. Examples of enforcing the G^1 continuity at a pole with Eq. 63.

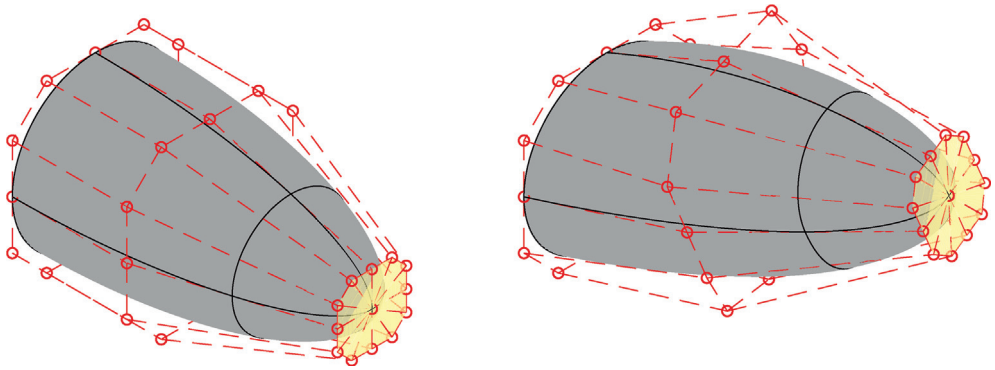

(a) Reference geometry. (b) Deformed geometry.

Fig. 2. Example of enforcing the G^1 continuity.

$$c(\mathbf{x})\Phi(\mathbf{x}) + \int_{\Gamma_b} \Phi(\mathbf{y}) \nabla_{\mathbf{y}} G(\mathbf{x},\mathbf{y}) \cdot \mathbf{n}(\mathbf{y}) \mathrm{d}\Gamma(\mathbf{y}) = \int_{\Gamma_b} G(\mathbf{x},\mathbf{y}) \nabla_{\mathbf{y}} \Phi(\mathbf{y}) \cdot \mathbf{n}(\mathbf{y}) \mathrm{d}\Gamma(\mathbf{y}) \tag{68}$$

where c is the solid angle [32, p. 12] divided by 4π; $\mathbf{x}$ is the evaluation point and $\mathbf{y}$ is the source point, both of them on Γ_b.

4.2.1. Regularization

The fundamental solution tends to infinity as the source point approaches the evaluation point, making Eq. 68 singular. The degree of this singularity is strong for the integrand on the left hand side $\nabla G \cdot \mathbf{n} \to O(1/r^2)$ whereas it is weak for the integrand on the right hand side $G \to O(1/r)$.

Weakly singular integrals can be integrated with special quadrature techniques, but strongly singular integrals can only be determined in the Cauchy principal value sense. A straightforward way of avoiding the computation of the Cauchy principal value is regularizing the strongly singular integrand using integral identities [33] or the "rigid body motion trick" applied to an infinite domain [34, p. 105].

Either of these two techniques allows getting an expression for the solid angle fraction that solely depends on the geometry:

$$c(\mathbf{x}) = 1 - \int_{\Gamma_b} \nabla_{\mathbf{y}} G(\mathbf{x},\mathbf{y}) \cdot \mathbf{n}(\mathbf{y}) \mathrm{d}\Gamma(\mathbf{y}) \tag{69}$$

Replacing Eq. 69 into Eq. 68 and rearranging terms, one obtains the regularized version of the boundary integral equation in which now the integrand of the left hand side is weakly singular too:

$$\Phi(\mathbf{x}) + \int_{\Gamma_b} [\Phi(\mathbf{y}) - \Phi(\mathbf{x})] \nabla_{\mathbf{y}} G(\mathbf{x},\mathbf{y}) \cdot \mathbf{n}(\mathbf{y}) \mathrm{d}\Gamma(\mathbf{y}) = \int_{\Gamma_b} G(\mathbf{x},\mathbf{y}) \nabla_{\mathbf{y}} \Phi(\mathbf{y}) \cdot \mathbf{n}(\mathbf{y}) \mathrm{d}\Gamma(\mathbf{y}) \tag{70}$$

4.2.2. Discretization

For the discretization of Eq. 70 we approximate the velocity potential with the NURBS basis functions used to represent the geometry:

$$\Phi(\mathbf{x}) = \sum_{j=1}^{n} R_j(\mathbf{x}) \hat{\phi}_j$$

where $\hat{\phi}_j$ are the control points of the NURBS representation of the velocity potential.

In Eq. 70, only the terms $\Phi(\mathbf{x})$ and $\Phi(\mathbf{y})$ of the left hand side need to be discretized. The term $\nabla_{\mathbf{y}}\Phi(\mathbf{y}) \cdot \mathbf{n}(\mathbf{y})$ of the right hand side is known from the impermeability boundary condition (Eq. 66). Then, introducing Eq. 71 and Eq. 66 into Eq. 70 and rearranging terms, the discretized boundary integral equation becomes:

$$\sum_{j=1}^{n}\Big\{R_j(\mathbf{x}) + \int_{\Gamma_b}\left[R_j(\mathbf{y}) - R_j(\mathbf{x})\right]\nabla_{\mathbf{y}}G(\mathbf{x},\mathbf{y})\cdot\mathbf{n}(\mathbf{y})\mathrm{d}\Gamma(\mathbf{y})\Big\}\hat{\phi}_j = \int_{\Gamma_b} G(\mathbf{x},\mathbf{y})\mathbf{v}_b(\mathbf{y})\cdot\mathbf{n}(\mathbf{y})\mathrm{d}\Gamma(\mathbf{y}) \tag{72}$$

We build the algebraic system of equations using the collocation method. Eq. 72 is evaluated at n collocation points $\mathbf{x}_i$ resulting in the following linear system:

$$\mathbf{A}\cdot\hat{\boldsymbol{\phi}} = \mathbf{b} \tag{73}$$

where:

$$A_{ij} = R_j(\mathbf{x}_i) + \int_{\Gamma_b}\left[R_j(\mathbf{y}) - R_j(\mathbf{x}_i)\right]\nabla_{\mathbf{y}}G(\mathbf{x}_i,\mathbf{y})\cdot\mathbf{n}(\mathbf{y})\mathrm{d}\Gamma(\mathbf{y}) \tag{74}$$

$$b_i = \int_{\Gamma_b} G(\mathbf{x}_i,\mathbf{y})\mathbf{v}_b(\mathbf{y})\cdot\mathbf{n}(\mathbf{y})\mathrm{d}\Gamma(\mathbf{y}) \tag{75}$$

The collocation points are chosen according to the physical image of the Greville abscissae, computed using Eq. 1, associated with each direction of the NURBS parametric space. For instance, along the parametric direction ξ, the Greville abscissae are defined as

$$\tilde{\xi}_k = \frac{1}{p}\left(\xi_{k+1} + \ldots + \xi_{k+p}\right) \tag{76}$$

where p is the NURBS degree and k goes from 1 to n, the total number of control points along this direction.

For problems with multi-patch geometries, some authors [35,36] modify the location of the first and last Greville abscissae to avoid collocating along sharp edges and/or having redundant collocation points. Though the geometries of this work are single-patch surfaces, we also move the first and last Greville abscissae inward the first and last knot span, respectively. In this way, we do not collocate at the poles of the geometries, and we avoid having redundant collocation points along their closing edges. We do this modification as follows

$$\tilde{\xi}_1\prime = \tilde{\xi}_1 + \beta\left(\tilde{\xi}_2 - \tilde{\xi}_1\right) \tag{77}$$

$$\tilde{\xi}_n\prime = \tilde{\xi}_n - \beta\left(\tilde{\xi}_n - \tilde{\xi}_{n-1}\right) \tag{78}$$

where $\beta \in [0,1)$ is a parameter that controls how much the collocation point is moved. This modification speeds up the evaluation of the integrals without compromising the quality of the solution from a practical point of view as we show in the Appendix A. We choose $\beta = 0.25$ for the simulations performed in this work.

4.2.3. Numerical evaluation of the integrals

The strategy for the numerical evaluation of the integrals closely follows the one described in [17]. Let $\mathbf{x}_i \in \Gamma_b$ be a collocation point defined by its parametric coordinates (ξ_i,η_i), $\Gamma_e \subset \Gamma_b$ be a region of integration defined by $[\xi_1,\xi_2]\times[\eta_1,\eta_2]$, d denote a representative measure of Γ_e in the physical space computed as

$$d = \max\left(\|\mathbf{r}(\xi_1,\eta_1) - \mathbf{r}(\xi_2,\eta_2)\|, \|\mathbf{r}(\xi_1,\eta_2) - \mathbf{r}(\xi_2,\eta_1)\|\right) \tag{79}$$

with $\mathbf{r}$ being the position vector. We distinguish three cases:

- Far-field: $(\xi_i,\eta_i) \notin \Gamma_e$ and $\|\mathbf{r}(\xi_i,\eta_i) - \mathbf{r}(\xi_s,\eta_s)\| > 2d$. We use the standard Gauss quadrature rule.
- Near-field: $(\xi_i,\eta_i) \notin \Gamma_e$ and $\|\mathbf{r}(\xi_i,\eta_i) - \mathbf{r}(\xi_s,\eta_s)\| \leqslant 2d$. The region of integration is initially split into four subregions (see Fig. 3 with $\epsilon_a = 0$) and in each of them we apply the Gauss quadrature rule modified with the Telles map [37].
- In-field: $(\xi_i,\eta_i) \in \Gamma_e$. The region of integration is initially split into eight subregions (see Fig. 3) and in each of them we apply the Gauss quadrature rule modified with the Telles map [37].

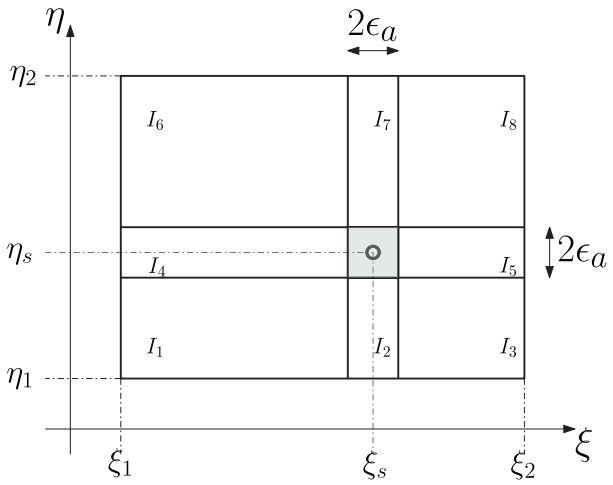

Fig. 3. Subdivision strategy for near-field ($\epsilon_a = 0$) and in-field regions.

where (ξ_s,η_s) represents the parametric coordinates of the closest point to $\mathbf{x}_i$ on Γ_e. For the three cases, we adaptively increase the number of quadrature points until the integral is computed with the desired number of significant digits n_{sd}. Besides this, for the near and in-field cases a quad-tree subdivision is recursively applied in each subregion in the event of not attaining the desired accuracy with 100 quadrature points.

In Fig. 3, ϵ_a is used to isolate the closest point to the collocation point, and it is defined as

$$\epsilon_a = \epsilon_r \min\left(\xi_2 - \xi_1, \eta_2 - \eta_1\right) \tag{80}$$

where $\epsilon_r \in [0,1)$ is a numerical parameter that controls the size of the cell isolating the point in question. The introduction of this parameter eases the convergence of the numerical quadrature. As we show in the Appendix A, this parameter does not compromise the accuracy of the solution for a given n_{sd} if $\epsilon_r < 10^{-n_{sd}}$. We choose $n_{sd} = 5$ and thereby $\epsilon_r = 5\cdot 10^{-6}$ for the simulations performed in this work.

5. Modal analysis of a submerged structure

5.1. Fluid modes

The harmonic vibration of a submerged structure induces motion in the surrounding fluid that can be considered irrotational because of the small displacements both systems undergo [7]. Assuming an inviscid and incompressible fluid, and recalling that the vibration of the structure is expressed in the form of a finite series of distortions in its principal modes, there exist a velocity potential that can be expressed as a finite series of fluid modes or velocity potentials [38]:

$$\Phi(\mathbf{x},t) = \sum_{k=1}^{m}\phi_k(\mathbf{x})z_k(t) \tag{81}$$

where m is the total number of *in-vacuo* vibrations modes under consideration.

Introducing Eq. 81 into Eq. 65 and considering that it must hold for an arbitrary value of m at any time instant, then each velocity potential must satisfy the Laplace equation:

$$\nabla^2\phi_k = 0 \tag{82}$$

The displacement of the body surface $\mathbf{d}$ results from the superposition of the modal displacements $\mathbf{d}_k$ induced by each *in-vacuo* vibration mode weighted with the generalized coordinates:

$$\mathbf{d}(\mathbf{x},t)=\sum_{k=1}^{m}\mathbf{d}_k(\mathbf{x})z_k(t) \tag{83}$$

The time derivative of $\mathbf{d}(\mathbf{x},t)$ defines the body surface velocity:

$$\mathbf{v}_b(\mathbf{x},t)=i\sum_{k=1}^{m}\omega_k\mathbf{d}_k(\mathbf{x})z_k(t) \tag{84}$$

Introducing Eq. 81 and Eq. 84 in Eq. 66 leads to the impermeability boundary condition that each velocity potential must satisfy on the body surface:

$$\frac{\partial\phi_k}{\partial n}=i\,\omega_k\,\mathbf{d}_k\cdot\mathbf{n} \tag{85}$$

Therefore, the solution of the fluid response is decomposed in a set of BVPs, one for each velocity potential ϕ_k, defined by Eq. 82, Eq. 85 and its corresponding far field condition. We solve these BVPs as described in the Section 4.

Finally, because of the linear character of the modal analysis technique, the impermeability boundary condition defined by Eq. 85 is applied on the reference configuration of the structure and not on its deformed configuration. Therefore, for all these BVPs the structure has the same geometry.

5.2. Generalized fluid force

The fluid inertial effects acting on the structure are modeled with the generalized added mass matrix. The fluid pressure acting on the structure can be computed with the linearized version of the Bernoulli's equation in which second-order terms in the velocity potential are neglected due to the small amplitude vibrations of the structure. This equation reads as follows:

$$p(\mathbf{x},t)\approx-\rho_w\frac{\partial\Phi(\mathbf{x},t)}{\partial t} \tag{86}$$

where ρ_w is the fluid density. Those readers interested in using Bernoulli's equation with its non-linear terms are referred to [39,40].

According to [38], the rth-component of the generalized fluid force acting on the structure can be expressed in the form

$$\tilde{f}_r(t)=-\int_{\Gamma_b}p(\mathbf{y},t)\mathbf{d}_r(\mathbf{y})\cdot\mathbf{n}(\mathbf{y})\mathrm{d}\Gamma(\mathbf{y}) \tag{87}$$

with $r=1,\dots,m$. Elaborating on Eq. 87, one can express the generalized fluid force as a generalized added mass times the acceleration of the modal coordinates:

$$\tilde{f}_r(t)=-\tilde{A}_{rk}\ddot{z}_k(t) \tag{88}$$

where

$$\tilde{A}_{rk}=\frac{\rho_w}{\omega_k^2}\mathrm{Re}\left[\int_{\Gamma_b}i\,\omega_k\,\phi_k(\mathbf{y})\mathbf{d}_r(\mathbf{y})\cdot\mathbf{n}(\mathbf{y})\mathrm{d}\Gamma(\mathbf{y})\right] \tag{89}$$

is the rth,kth-coefficient of the generalized added mass matrix $\tilde{\mathbf{A}}$ associated with the rth-mode, and represents the coupled effect due to the harmonic oscillation of unit amplitude in the kth-mode [38]. Moreover, a close examination of Eq. 89, Eq. 85, and Eq. 73 shows that $\tilde{\mathbf{A}}$ is frequency-independent [4,9].

5.3. In-water eigenvalue analysis

In the absence of structural damping, and under the sole action of the generalized fluid force defined by Eq. 88, the generalized equation of motion has the form

$$\left(\tilde{\mathbf{M}}+\tilde{\mathbf{A}}\right)\cdot\ddot{\mathbf{z}}+\tilde{\mathbf{K}}\cdot\mathbf{z}=\mathbf{0} \tag{90}$$

Since the free response of the system is harmonic, the solution to Eq. 90 can be expressed as $\mathbf{z}=\hat{\boldsymbol{\psi}}e^{i\hat{\omega}t}$, leading to a generalized eigenproblem

$$\tilde{\mathbf{K}}\cdot\hat{\boldsymbol{\psi}}=\hat{\omega}^2\left(\tilde{\mathbf{M}}+\tilde{\mathbf{A}}\right)\cdot\hat{\boldsymbol{\psi}} \tag{91}$$

whose solutions are the wet natural frequencies $\hat{\omega}$ and the wet vibration modes $\hat{\boldsymbol{\psi}}$ in generalized coordinates. The coordinates of the control points of the wet vibration modes are computed multiplying the *in-vacuo* modal matrix and the in-water modal matrix [10].

6. Benchmark examples

In the following, we use the methodology described in Section 5 to compute the dynamic characteristics of unconstrained and closed shells of revolution. In order to validate our implementation, we have selected three test cases for which there are reference results publicly available in the literature. The three test cases are:

- Unconstrained sphere: theoretical reference values presented by Junger and Feit [41, p. 257];
- Unconstrained cylinders:
  - Cylinder A: numerical reference values presented by Everstine [4], Gilroy [42], Monterrubio and Krysl [10];
  - Cylinder B: theoretical and experimental reference values presented by Randall [43], and numerical reference values by Gilroy [42], Monterrubio and Krysl [10].

In this section, E stands for the Young's modulus; ν for the Poisson's ratio; L and R for the outer shell length and radius; L_{ms} and R_{ms} for the midsurface shell length and radius; h for the shell thickness; and ρ_s for the material density.

6.1. Unconstrained sphere

This test case shows the results for the dry and wet natural frequencies and vibration modes of a hollow spherical shell. A complete convergence study of the natural frequencies is carried out, both in dry and wet conditions, assessing the computational advantage of using non-matching parametrizations between the structural and the fluid problems when computing the wet natural frequencies.

This analysis focuses on the modes of order $n=2,\dots,9$. For each value of n, there are $2n+1$ eigenmodes sharing the same eigenfrequency, one axisymmetric and $2n$ non-axisymmetric modes. Therefore, a total of 102 eigenmodes have to be computed.

We benchmark the computed frequencies against their theoretical values [41, p. 257]. These reference values were determined neglecting flexural effects and considering that the fluid surrounding the sphere is compressible. For this example, the results are presented in terms of the dimensionless angular frequency

$$\tilde{\omega}=\frac{\omega R_{ms}}{c_p} \tag{92}$$

where ω is the angular frequency and

$$c_p=\sqrt{\frac{E}{\rho_s(1-\nu^2)}} \tag{93}$$

is the low frequency phase velocity of the compressional waves in an elastic plate.

Finally, the shell material properties are $E=196$ GPa, $\nu=0.30$ and $\rho_s=7670$ kg/m^3, and the density of the water is $\rho_w=1000$ kg/m^3.

6.1.1. Parametrization of the geometry

The spherical shell has $R_{ms} = 3.0$ m and $h = 0.03$ m. Its geometry is described by a single bi-quadratic NURBS surface with 45 control points [19, p. 347] and is illustrated in Fig. 4. This parametrization is the coarsest level that we use in the analysis.

6.1.2. Results

We have performed a convergence study of the natural frequencies of the sphere, both in dry and wet conditions. These results are presented in Fig. 5, 7 and 8, in which n is the mode identifier, n_{cp} is the number of degrees of freedom or control points, and ϵ is the relative error of $\tilde{\omega}$, computed as

$$\epsilon = \frac{\tilde{\omega}_{ref} - \tilde{\omega}_{com}}{\tilde{\omega}_{ref}} \tag{94}$$

where $\tilde{\omega}_{ref}$ is the reference value taken from [41] and $\tilde{\omega}_{com}$ is the computed value.

For this convergence study, we have excluded the shell bending stiffness from Eq. 53 to get a pure membrane behavior as in [41]. For the sake of conciseness, we only present the results for the bi-quadratic and bi-cubic NURBS parametrizations concerning the modes $2, 3, 8$ and 9 in dry conditions and for the modes 8 and 9 in wet conditions.

Fig. 5 shows the convergence plots in dry conditions where one can see that the four modes exhibit similar orders of convergence. We highlight that the reference results in [41] are provided with only three significant digits. For this reason and as can be seen in Fig. 5, the convergence curves level off at a relative error approximately equal to 10^{-4}.

It is known that the higher the mode order, the larger the number of degrees of freedom needed to achieve convergence. Fig. 5 (b) is a clear example of it when comparing, for instance, modes 2 and 8. The latter needs approximately ten times more control points than the former for a similar relative error at convergence. If one is interested only in the low order modes, a coarse parametrization already allows us getting a converged solution and a good representation of the vibration patterns [44] as shown in Fig. 6.

For the wet convergence analysis we have followed two approaches. In the first one, the NURBS spaces used to discretize the displacements and the velocity potential are refined simultaneously, and therefore, they match each other. Fig. 7 shows the results with this first approach.

In the second approach, the NURBS spaces of the displacements and the velocity potential are independent. Contrary to the case of the standard FEM and BEM for non-matching meshes, within the isogeometric framework there is no need to interpolate the solution fields at the body surface. This is because the geometry is the same for both numerical methods and the solution fields have a continuous representation over the body surface.

The way we proceed in this second approach is the following. First, only one dry eigenvalue analysis is performed, with the displacement field discretized by a bi-septic NURBS plus two levels of knot refinement (861 control points). With this parametrization, the relative error of all the dry eigenfrequencies is below 10^{-3}. Then, the eigenmodes of this dry analysis are used in all the subsequent fluid analyses in which the NURBS representation of the velocity potential is refined starting from a bi-quadratic NURBS with 45 control points. Fig. 8 shows the results for this second approach.

Let us compare Fig. 7 and Fig. 8 focusing on, for instance, the mode 8 and $(p, q) = (2, 2)$. One can see that to attain a relative error of 10^{-2}, with the first approach around 1000 control points are needed whereas with the second approach 400 control points suffice to discretize the velocity potential. The total computational cost of this kind of simulation is completely driven by the fluid analysis, and hence any significant reduction in the number of control points of the velocity potential is largely beneficial. This is achieved with the second approach, and consequently, it is more efficient than the first one for a given accuracy.

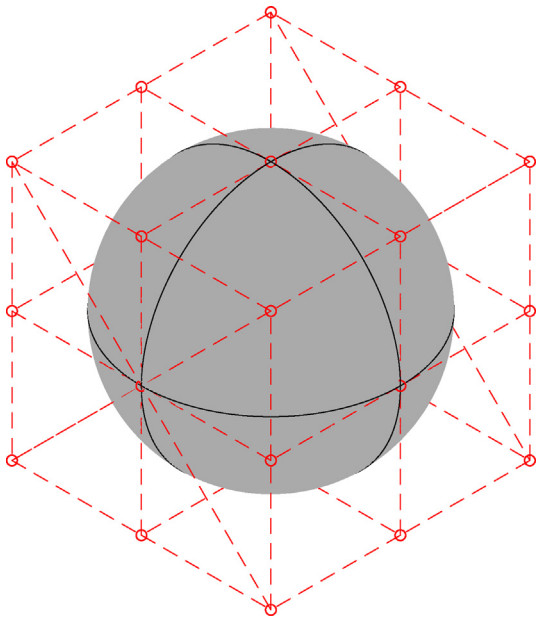

Fig. 4. Bi-quadratic NURBS modelling a sphere.

The results presented hereafter correspond to a parametrization with a bi-septic NURBS for the displacement field, and with a bi-quintic NURBS for the velocity potential field. For both fields, we also apply two levels of knot refinement. The number of control points is 861 for the displacement field and 561 for the velocity potential field. The frequencies have been computed with and without bending stiffness to assess how it influences the results.

The comparison between theoretical and computed dry frequencies is shown in Fig. 9. One can notice that the bending stiffness influences the solution by slightly increasing the frequency of the modes $n \geqslant 5$. When this stiffness is neglected, the numerical values completely match the theoretical counterparts.

Fig. 10 illustrates the generatrix[1] of the dry axisymmetric vibration modes without bending stiffness. The mode of order $n = 0$ is used to represent the reference generatrix line of the sphere.

Next, Fig. 11 shows the same comparison as before but now for the wet natural frequencies. The agreement for these frequencies is fairly good, especially for modes of order $n \geqslant 4$ for which the discrepancy is below 4% in the case of the membrane model. The modes of order 2 and 3 exhibit a discrepancy of 9.9% and 9.2%, respectively, regardless of whether or not the bending stiffness is vanished. For these two modes, further investigations are needed to identify the source of these discrepancies. We think that it is a consequence of the incompressible fluid assumption because the fluid compressibility is responsible for the radiation damping, which decreases as the complexity of the mode shape increases [45].

6.2. Unconstrained cylinders

These test cases show the results for the dry and wet natural frequencies and vibration modes of two hollow cylindrical shells with different aspect ratio and thickness to radius ratio. These

[1] Line that is revolved around an axis of revolution to produce a surface.

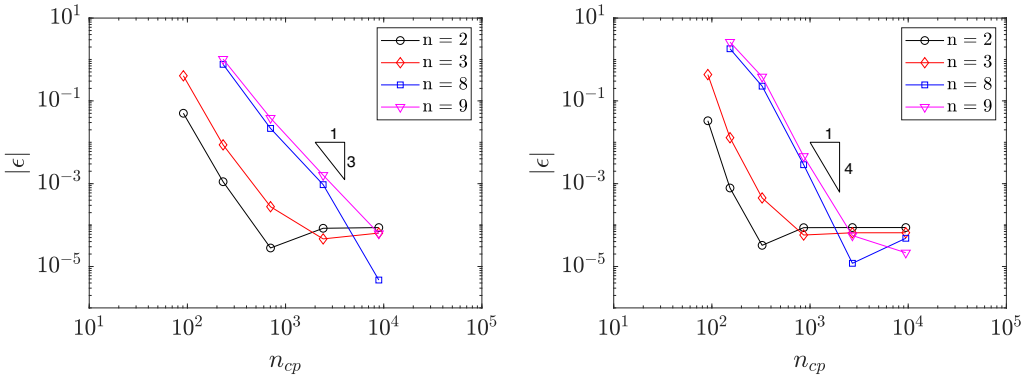

(a) $(p, q) = (2, 2)$ (b) $(p, q) = (3, 3)$

Fig. 5. Unconstrained sphere: convergence of the relative error of the dry natural frequencies for the modes 2, 3, 8 and 9. (a): bi-quadratic parametrization. (b): bi-cubic parametrization.

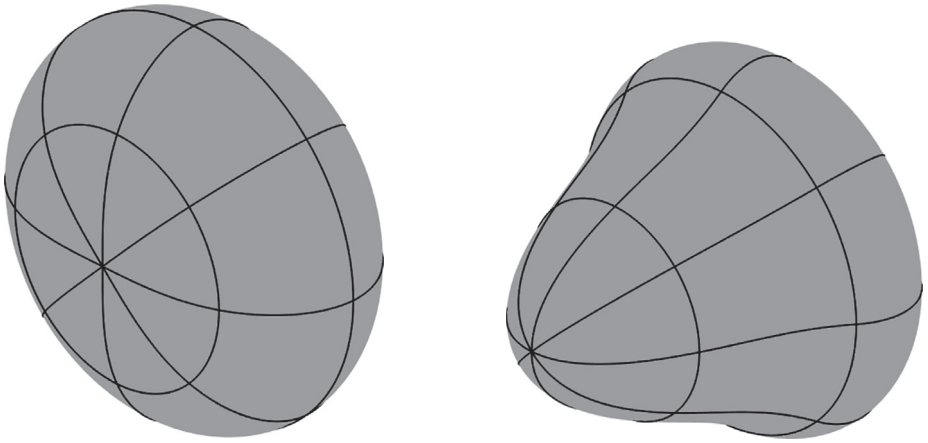

(a) $n = 2$ (b) $n = 3$

Fig. 6. Unconstrained sphere: axisymmetric vibration modes 2 and 3 in dry conditions. Bi-cubic NURBS, with one level of knot refinement (153 control points).

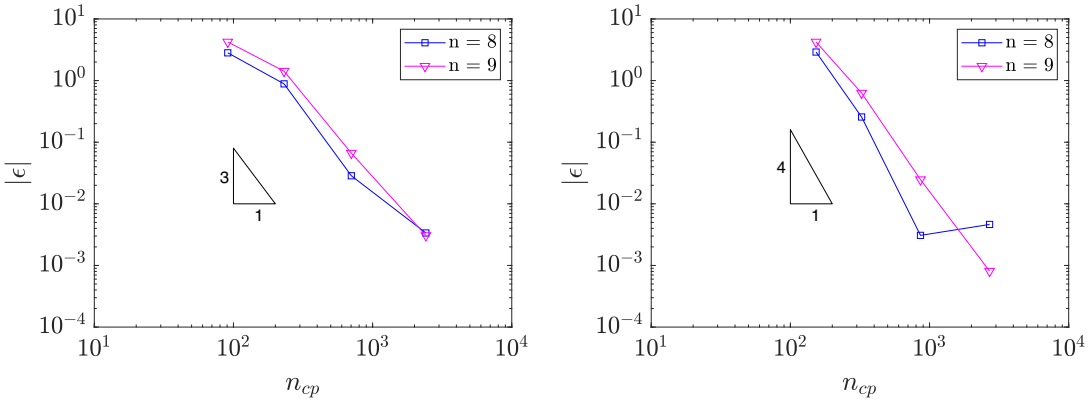

(a) $(p, q) = (2, 2)$ (b) $(p, q) = (3, 3)$

Fig. 7. Unconstrained sphere: convergence of the relative error of the wet natural frequencies for the modes 8 and 9 with matching parametrizations. (a): bi-quadratic parametrization. (b): bi-cubic parametrization.

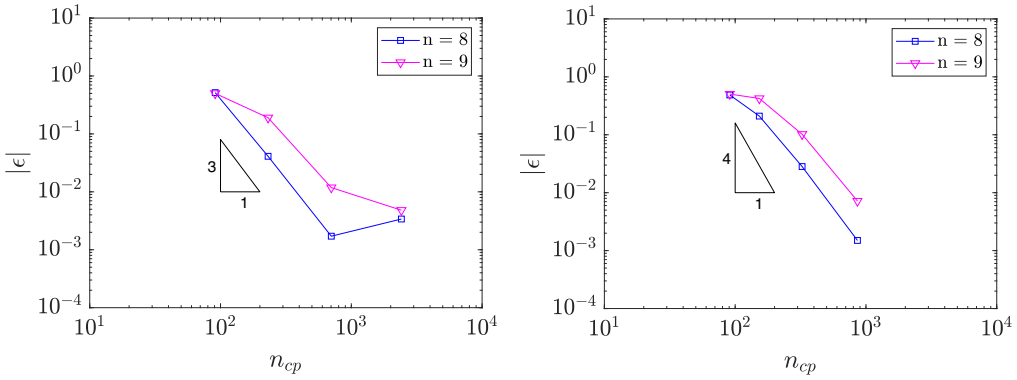

(a) $(p, q) = (2, 2)$ (b) $(p, q) = (3, 3)$

Fig. 8. Unconstrained sphere: convergence of the relative error of the wet natural frequencies for the modes 8 and 9 with non-matching parametrizations. (a): bi-quadratic parametrization. (b): bi-cubic parametrization.

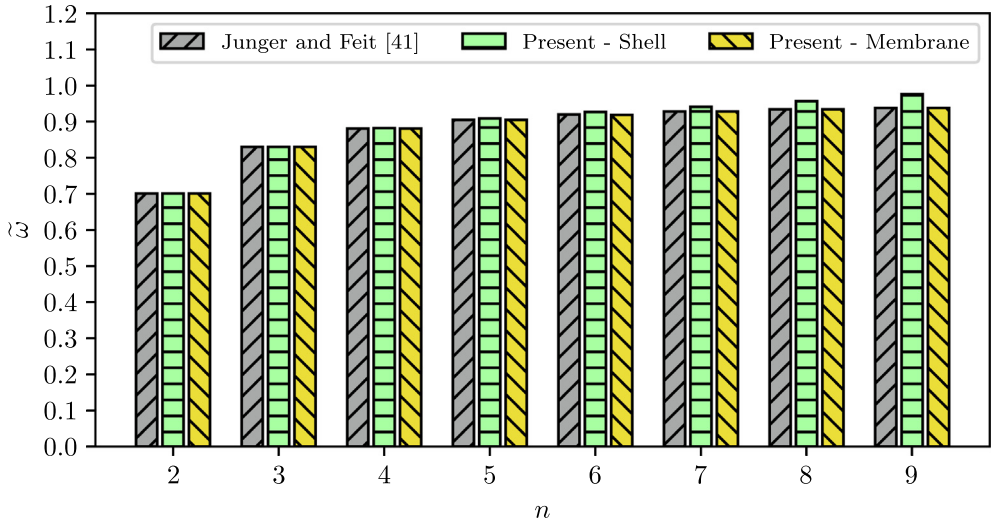

Fig. 9. Unconstrained sphere: dry natural frequencies.

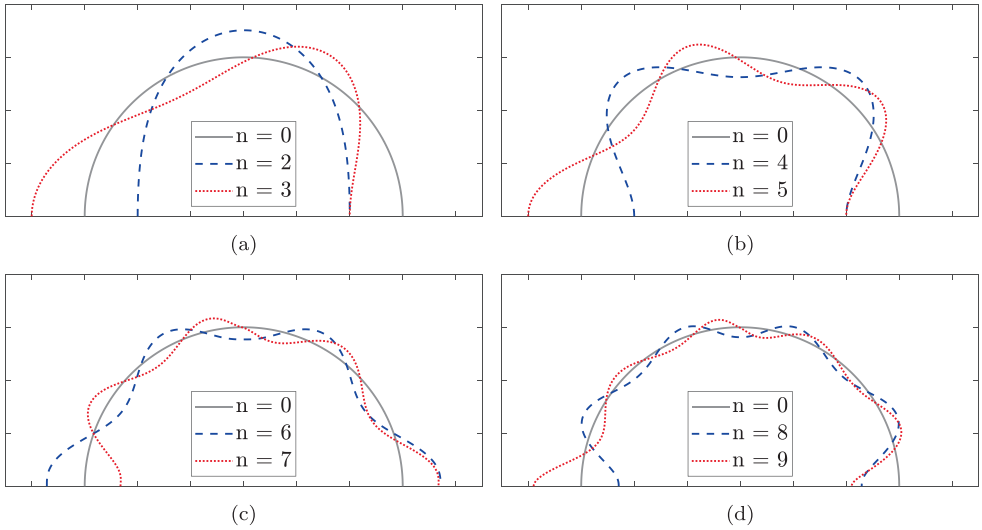

Fig. 10. Unconstrained sphere: generatrices of the axisymmetric dry eigenmodes without bending stiffness.

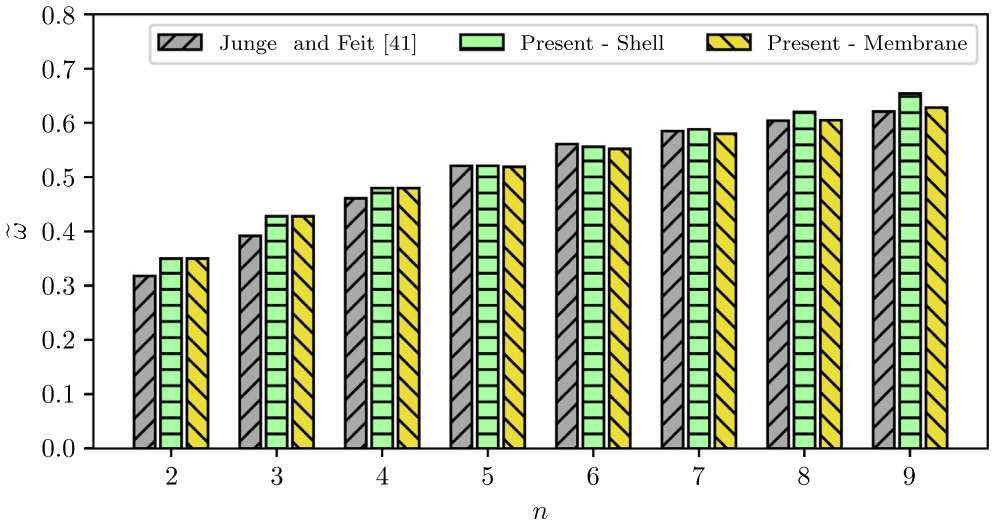

Fig. 11. Unconstrained sphere: wet natural frequencies.

Table 1
Main dimensions and material properties of the unconstrained cylinders.

Cylinder	L [m]	R [m]	h [m]	E [GPa]	ν [–]	ρ_s [kg/m^3]
A	60.00	5.00	0.050	196	0.30	7900
B	1.284	0.18	0.003	207	0.29	7750

analyses focus on the first 16 vibration modes, rigid body modes excluded. Table 1 summarizes the main dimensions and shell material properties for each cylinder. For both cases, the density of the water is $\rho_w = 1000$ kg/m^3.

6.2.1. Parametrization of the geometry

The geometry of the cylinder is described by a single-patch NURBS surface. This geometry is constructed as a surface of revolution using the generatrix line depicted in Fig. 12. It is a cubic NURBS curve, with a non-uniform knot vector, and its 12 control points have unit weight. The knot vector is computed using a chordal-length parametrization and the algorithm described in [46].

With this generatrix line, the cylinder will have a small fillet between the flat end caps and the wall, and thereby no sharp edges will be present in the geometry. The resulting NURBS surface modeling the cylinder has 108 control points, it is quadratic in the circumferential direction and is cubic in the axial direction.

6.2.2. Results

As for the sphere test case, a different NURBS parametrization is used for the displacement and the velocity potential fields. For the *in-vacuo* eigenvalue analysis, the NURBS surface is made sextic in the circumferential direction and quintic in the axial direction. For the in-water analysis, the NURBS surface is made quintic in the circumferential direction and quartic in the axial direction. For both solution fields, the knot vector in the circumferential direction is uniformly refined twice, and the knot vector in the axial direction is locally refined. After these operations of degree elevation and knot insertion, the final number of control points in 1443 for the displacements and 990 for the velocity potential.

We classify the vibration modes of a cylinder as (m,n) or (e). The axial wave number is m, while n is the circumferential wave number. The end-plate modes are identified with an e followed by the number of nodal diametrical lines. The first 16 dry vibration

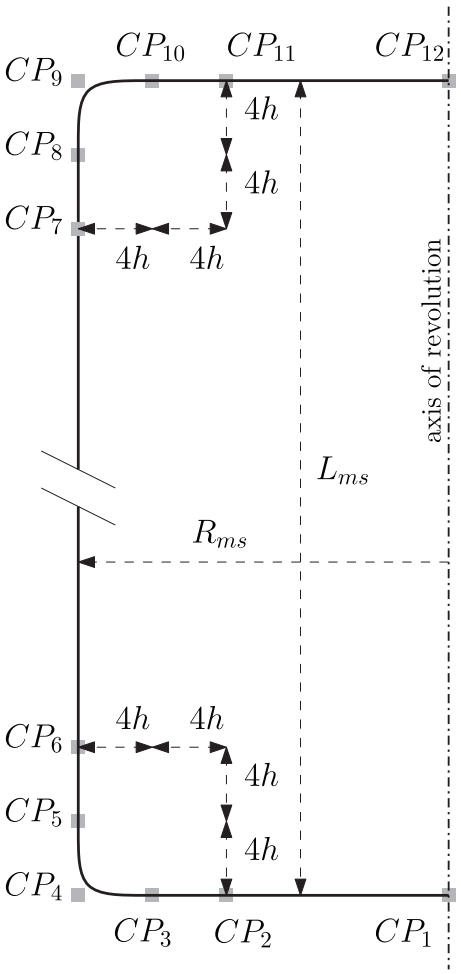

Fig. 12. Generatrix for a single-patch NURBS cylinder.

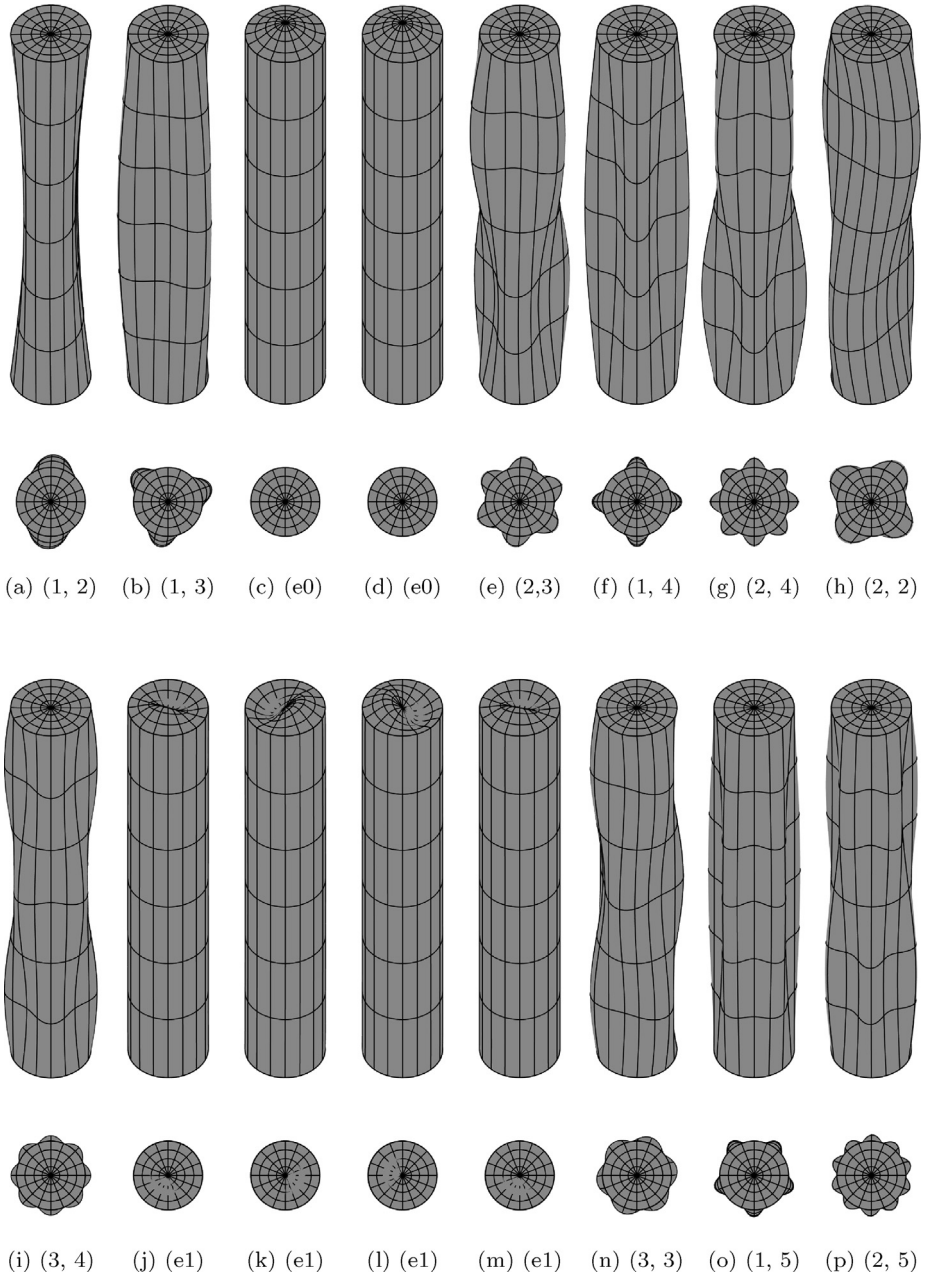

Fig. 13. Cylinder A: dry eigenmodes.

modes are illustrated in Fig. 13 and Fig. 14 for the cylinders A and B, respectively. In these figures, the two $e0$ modes do not correspond to a repeated eigenfrequency (see Appendix B). The difference between them is that in the first case, both end-plates deform outward (symmetric mode), whereas in the second case, one end-plate deforms outward and the other one inward (asymmetric mode).

Figs. 15–18 compare the computed dry and wet natural frequencies with the values published by the different authors. In these figures we show only the results for the modes that were computed by all the authors. For the frequencies of the other modes, please see Appendix B.

In general, there is a good agreement with the results reported in the literature, with the largest discrepancies happening for the end-plate mode $e0$.

7. Conclusions

A high-order numerical scheme based on the isogeometric formulations of the FEM and the BEM, combined with the modal superposition approach, has been applied to the assessment of the dynamic characteristics of submerged thin-walled structures. The geometry preserving property of the NURBS refinement strategies has been exploited in the analyses. We have used a finer discretization for the structural problem than for the fluid problem without the need for a projection scheme as it would have been required by the standard formulations of the FEM and the BEM.

On the structural problem side, we have proposed a novel master–slave strategy to enforce the G^1 continuity at the pole of a surface of revolution. With the use of the area coordinates, we have shown how to exactly enforce the coplanarity of the control points

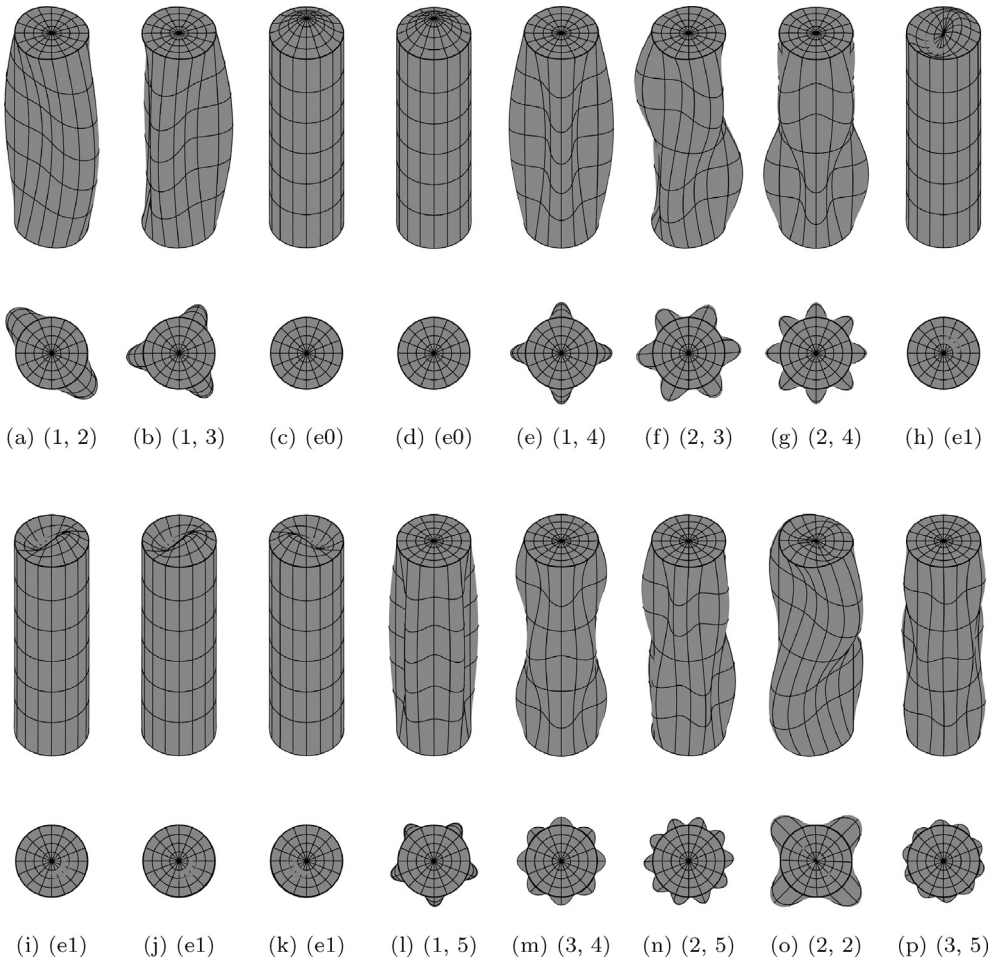

Fig. 14. Cylinder B: dry eigenmodes.

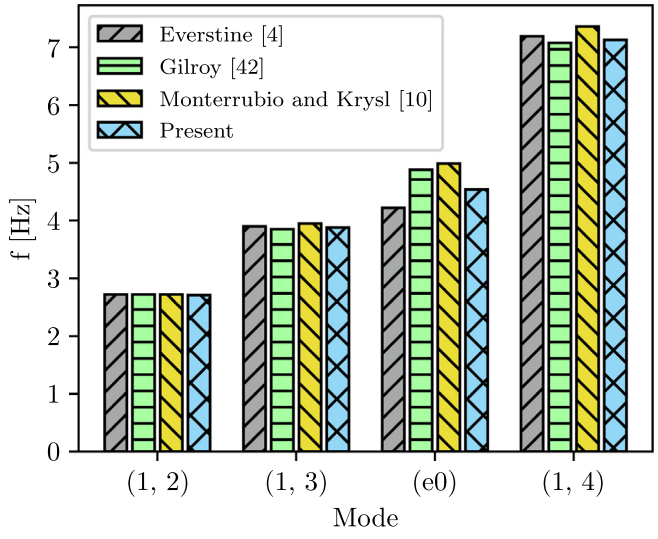

Fig. 15. Cylinder A: dry frequencies - comparison among authors.

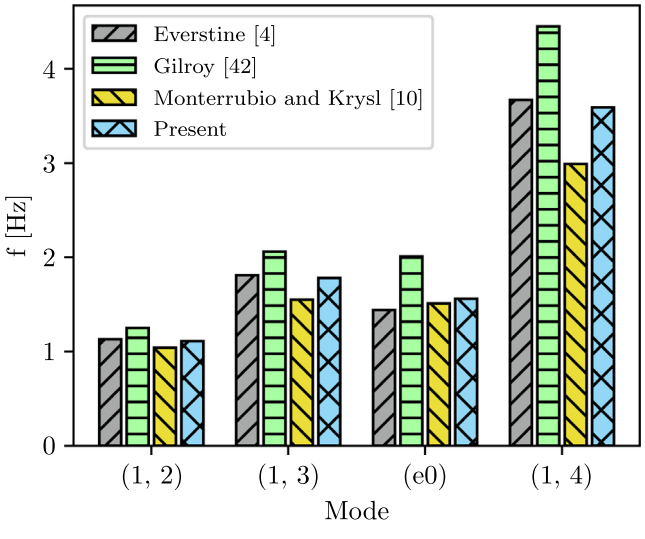

Fig. 16. Cylinder A: wet frequencies - comparison among authors.

that govern this continuity. On the fluid problem side, we have used a weakly-singular boundary integral equation in contrast to the standard strongly-singular one commonly used in the application of the isogeometric analysis to potential flow problems.

This numerical scheme has been implemented and benchmarked against reference results available in the literature for a submerged sphere and two submerged cylinders. They show a good agreement for both the *in-vacuo* and wet conditions, and the differences lie within the expected range when comparing numerical with theoretical or experimental results. Moreover, these satisfactory numerical results have been computed with a relatively low number of degrees of freedom.

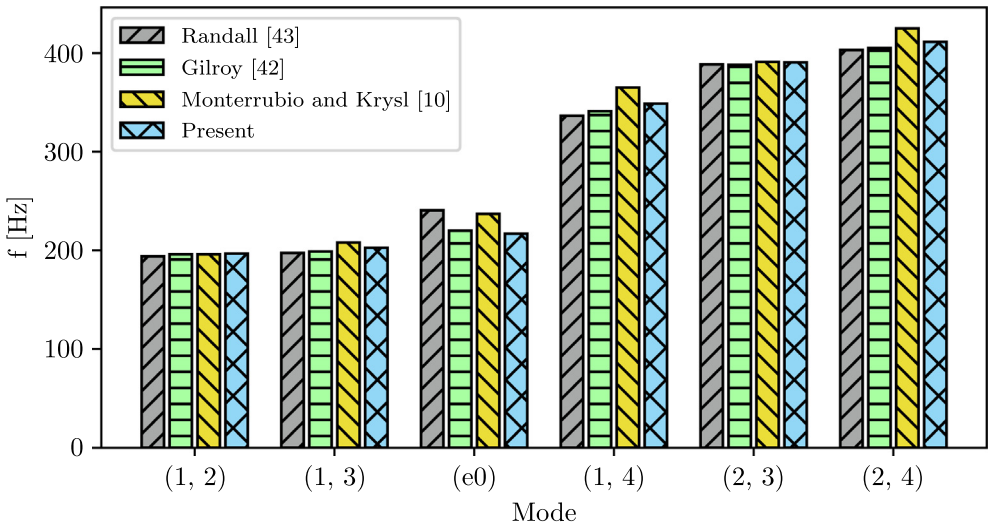

Fig. 17. Cylinder B: dry frequencies - comparison among authors.

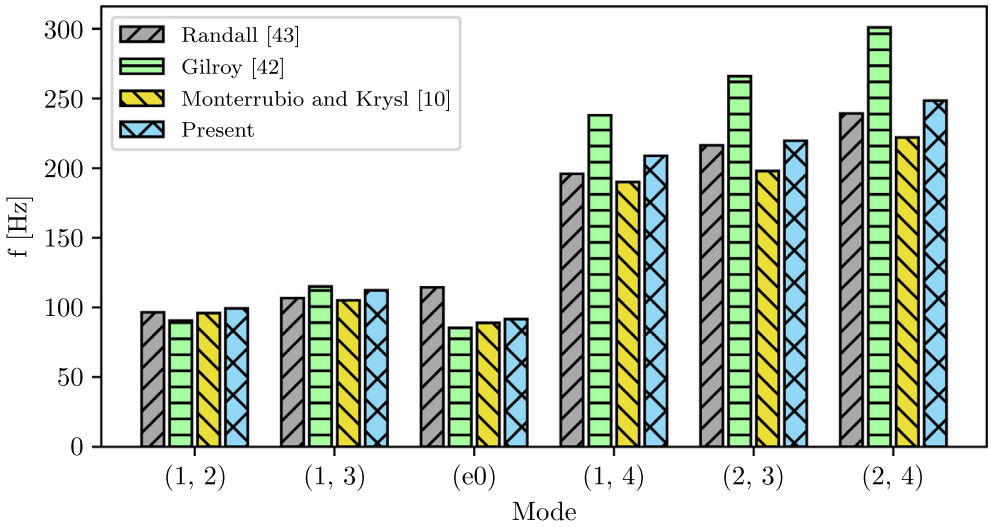

Fig. 18. Cylinder B: wet frequencies - comparison among authors.

Declaration of Competing Interest

The authors declare that they have no known competing financial interests or personal relationships that could have appeared to influence the work reported in this paper.

Acknowledgments

The present work was partly supported by the FleksProp project, which is a cooperation between Kongsberg Maritime, the Norwegian University of Science and Technology, and SINTEF Ocean. This research was funded by Kongsberg Maritime and the Research Council of Norway [Grant No. 267495/O80].

Appendix A. Selection of the numerical parameters β and ϵ_r

In this appendix, we present two parametric studies that we have carried out to choose the values of the numerical parameters β and ϵ_r introduced in Section 4.2. The test case is a sphere in a free stream for which the velocity potential has a closed-form solution (for instance, see [30, p. 67]). For this test case, we study the influ-

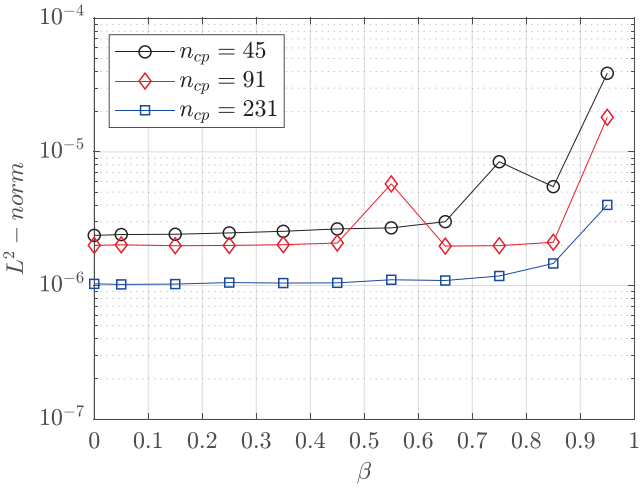

Fig. A.19. Influence of β on the L^2-norm of the relative error of the perturbation potential.

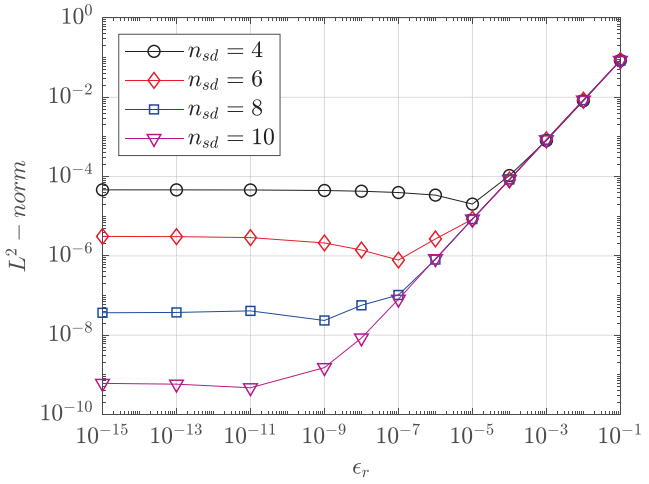

Fig. A.20. Influence of ϵ_r on the L^2-norm of the relative error of the perturbation potential.

ence of these parameters on the L^2-norm of the relative error of the perturbation potential. The sphere has a unit radius and the free stream speed is 1.0 m/s.

The first study concerns the influence of the parameter β. The sphere is represented with a bi-quadratic NURBS surface, and three levels of knot refinement are considered leading to the following number of control points (n_{cp}): 45, 91, and 231. Integrals are computed with 6 significant digits and $\epsilon_r = 5 \cdot 10^{-7}$.

Fig. A.19 shows the results for this study. One can conclude that if $\beta \leqslant 0.4$, the L^2-norm of the solution is not sensitive to this parameter from a practical viewpoint. Moreover, the influence of this parameter decreases as the NURBS parametric space is refined.

Next, we proceed to analyze the influence of the parameter ϵ_r. The sphere is represented with a bi-quadratic NURBS surface including one level of knot refinement (91 control points). Integrals are computed with 4, 6, 8 and 10 significant digits (n_{sd}), ϵ_r ranges from 10^{-15} to 10^{-1}, and $\beta = 0.25$.

Fig. A.20 shows the results for this second analysis. It becomes noticeable that for each n_{sd} the behavior of the L^2-norm resembles a bi-linear function, being constant for $\epsilon_r < 10^{-n_{sd}}$ and then increasing linearly with ϵ_r in a logarithmic scale.

Appendix B. Tabulated natural frequencies for the cylinders

Table B.2 and Table B.3 summarize the values of the dry and wet natural frequencies for the cylinders A and B, respectively. In Table B.2 all the values were determined numerically. In Table B.3 all the values were determined numerically with the exception of the reference [43]. In this reference, the values were determined experimentally except for the dry modes $(2,2)$ and

Table B.2
Dry and wet natural frequencies [Hz] of the cylinder A.

Mode	Reference - Dry				Reference - Wet			
(m, n)	[4]	[42]	[10]	Present	[4]	[42]	[10]	Present
(1, 2)	2.72	2.72	2.72	2.71	1.13	1.25	1.04	1.11
(1, 3)	3.90	3.85	3.95	3.88	1.81	2.06	1.55	1.78
(e0)	4.22	4.88	4.99	4.54	1.44	2.01	1.51	1.56
	–	–	5.11	4.65	–	–	1.88	1.96
(2, 3)	–	–	5.86	5.83	–	–	2.31	2.69
(1, 4)	7.19	7.08	7.36	7.13	3.67	4.45	2.99	3.59
(2, 4)	–	–	7.86	7.64	–	–	3.21	3.86
(2, 2)	–	–	–	9.04	–	–	–	3.79
(3, 4)	9.34	9.27	–	9.29	4.82	6.05	–	4.74
(e1)	9.20	10.80	–	9.61	4.26	6.01	–	4.42
(3, 3)	10.40	10.30	–	10.35	4.93	5.96	–	4.86
(1, 5)	11.60	11.40	–	11.59	6.38	–	–	6.27
(2, 5)	–	–	–	11.79	–	–	–	6.40

Table B.3
Dry and wet natural frequencies [Hz] of the cylinder B.

Mode	Reference - Dry				Reference - Wet			
(m, n)	[43]	[42]	[10]	Present	[43]	[42]	[10]	Present
(1, 2)	193.9	196.0	196.0	196.8	96.4	90.5	96.0	99.3
(1, 3)	197.4	199.0	208.0	202.7	106.7	115.0	105.0	112.2
(e0)	240.7	220.0	237.0	217.0	114.4	85.3	88.9	91.6
	270.5	228.0	245.0	225.2	128.6	85.3	112.0	116.6
(1, 4)	336.5	341.0	365.0	348.7	195.9	238.0	190.0	208.8
(2, 3)	387.0	388.0	391.0	390.5	216.3	266.0	198.0	219.7
	389.9	–	–	–	–	–	–	–
(2, 4)	403.1	405.0	425.0	411.4	239.2	301.0	222.0	248.4
(e1)	389.3	–	–	–	252.9	–	–	251.6
	402.2	–	–	–	–	–	–	–
	422.6	–	–	–	–	–	–	–
	457.0	–	–	455.8	–	–	–	–
(1, 5)	537.1	546.0	–	559.5	360.4	–	–	356.3
(3, 4)	564.7	570.0	584.0	574.8	344.5	–	308.0	351.9
(2, 5)	568.6	575.0	–	587.0	376.9	–	–	375.7
(2, 2)	653.2	–	–	639.4	327.8	340.0	–	334.6
(3, 5)	662.0	–	–	660.8	422.4	–	–	426.9

$(3,5)$, and the wet modes $(1,5)$, $(3,4)$, $(2,5)$, $(2,2)$ and $(3,5)$ that were computed analytically.

References

[1] Deruntz JA, Geers TL. Added mass computation by the boundary integral method. Int. J. Numer. Meth. Eng. 1978;12:531–50.
[2] Everstine G. Finite element formulations of structural acoustics problems. Computers & Structures 1997;65:307–21.
[3] Zienkiewicz OC, Newton RE. Coupled vibrations of a structure submerged in a compressible fluid. In: Symposium on Finite Element Techniques. Germany: University of Stuttgart; 1969.
[4] Everstine GC. Prediction of low frequency vibrational frequencies of submerged structures. J. Vib. Acoust. 1991;113:187–91.
[5] Changjun Z, Chuanxing B, Haibo C, Chuanzeng Z. Fluid-structure interaction eigenvalue analysis by using a coupled FE-BE solver. In: The 8th International Conference on Computational Methods (ICCM2017).
[6] Zheng C-J, Bi C-X, Zhang C, Gao H-F, Chen H-B. Free vibration analysis of elastic structures submerged in an infinite or semi-infinite fluid domain by means of a coupled FE–BE solver. J. Comput. Phys. 2018;359:183–98.
[7] Antoniadis I, Kanarachos A. A decoupling procedure for the modal analysis of structures in contact with incompressible fluids. Communications in Applied Numerical Methods 1987;3:507–17.
[8] Ergin A, Temarel P. Free vibration of a partially liquid-filled and submerged, horizontal cylindrical shell. J. Sound Vib. 2002;254:951–65.
[9] Ergin A, Ugurlu B. Linear vibration analysis of cantilever plates partially submerged in fluid. J. Fluids Struct. 2003;17:927–39.
[10] Monterrubio LE, Krysl P. Natural frequencies of submerged structures using an efficient calculation of the added mass matrix in the boundary element method. J. Vib. Acoust. 2019;141.
[11] Sepehrirahnama S, Ong ET, Lee HP, Lim K-M. Fast computation for vibration study of partially submerged structures using low resolution hydrodynamic model. J. Fluids Struct. 2019;91:102756.
[12] Yildizdag ME, Ardic IT, Demirtas M, Ergin A. Hydroelastic vibration analysis of plates partially submerged in fluid with an isogeometric FE-BE approach. Ocean Eng. 2019;172:316–29.
[13] Yildizdag ME, Ardic IT, Kefal A, Ergin A. An isogeometric FE-BE method and experimental investigation for the hydroelastic analysis of a horizontal circular cylindrical shell partially filled with fluid. Thin-Walled Structures 2020;151:106755.
[14] Hughes T, Cottrell J, Bazilevs Y. Isogeometric analysis: CAD, finite elements, NURBS, exact geometry and mesh refinement. Comput. Methods Appl. Mech. Eng. 2005;194:4135–95.
[15] J. Cottrell, A. Reali, Y. Bazilevs, T. Hughes, Isogeometric analysis of structural vibrations, Computer Methods in Applied Mechanics and Engineering 195 (2006) 5257 – 5296. John H. Argyris Memorial Issue. Part II.
[16] Politis C, Ginnis AI, Kaklis PD, Belibassakis K, Feurer C. An isogeometric BEM for exterior potential-flow problems in the plane. In: 2009 SIAM/ACM Joint Conference on Geometric and Physical Modeling, SPM'09. New York, NY, USA: Association for Computing Machinery; 2009. p. 349–54.
[17] Belibassakis K, Gerostathis T, Kostas K, Politis C, Kaklis P, Ginnis A, Feurer C. A BEM-isogeometric method for the ship wave-resistance problem. Ocean Eng. 2013;60:53–67.
[18] Kiendl J, Bletzinger K, Linhard J, Wüchner R. Isogeometric shell analysis with Kirchhoff-Love elements. Comput. Methods Appl. Mech. Eng. 2009;198:3902–14.
[19] Piegl L, Tiller W. The NURBS Book. second ed. New York, NY, USA: Springer-Verlag; 1996.
[20] Cox MG. The Numerical Evaluation of B-Splines. IMA Journal of Applied Mathematics 1972;10:134–49.
[21] Kiendl JM. Isogeometric Analysis and Shape Optimal Design of Shell Structures Ph.D. thesis. Lehrstuhl für Statik: Technischen Universität München; 2010.
[22] Kiendl J, Hsu M-C, Wu MC, Reali A. Isogeometric Kirchhoff-Love shell formulations for general hyperelastic materials. Comput. Methods Appl. Mech. Eng. 2015;291:280–303.
[23] Paultre P. Dynamics of Structures. John Wiley & Sons Ltd; 2011.
[24] Kiendl J, Bazilevs Y, Hsu M-C, Wüchner R, Bletzinger K-U. The bending strip method for isogeometric analysis of Kirchhoff-Love shell structures comprised of multiple patches. Comput. Methods Appl. Mech. Eng. 2010;199:2403–16.
[25] Breitenberger M, Apostolatos A, Philipp B, Wüchner R, Bletzinger K-U. Analysis in computer aided design: Nonlinear isogeometric b-rep analysis of shell structures. Comput. Methods Appl. Mech. Eng. 2015;284:401–57.
[26] Lei Z, Gillot F, Jezequel L. A c0/g1 multiple patches connection method in isogeometric analysis. Appl. Math. Model. 2015;39:4405–20.
[27] Herrema AJ, Johnson EL, Proserpio D, Wu MC, Kiendl J, Hsu M-C. Penalty coupling of non-matching isogeometric Kirchhoff-Love shell patches with application to composite wind turbine blades. Comput. Methods Appl. Mech. Eng. 2019;346:810–40.
[28] Kleiss SK, Pechstein C, Jüttler B, Tomar S. IETI – Isogeometric Tearing and Interconnecting. Comput. Methods Appl. Mech. Eng. 2012;247–248:201–15.
[29] E. Oñate, Structural Analysis with the Finite Element Method. Linear Statics. Volume 1: Basis and Solids, first ed., Springer Netherlands, 2009.
[30] Katz J, Plotkin A. Low-Speed Aerodynamics, Cambridge Aerospace Series. second ed. Cambridge University Press; 2001.
[31] Chatjigeorgiou IK. Analytical Methods in Marine Hydrodynamics. Cambridge University Press; 2018.
[32] Kellogg OD. Foundations of potential theory. Springer; 1967.
[33] Liu Y, Rudolphi T. Some identities for fundamental solutions and their applications to weakly-singular boundary element formulations. Eng. Anal. Boundary Elem. 1991;8:301–11.
[34] Beer G, Marussig B, Duenser C. The Isogeometric Boundary Element Method, Lecture Notes in Applied and Computational Mechanics. Springer Nature; 2020.
[35] Wang Y, Benson D. Multi-patch nonsingular isogeometric boundary element analysis in 3D. Comput. Methods Appl. Mech. Eng. 2015;293:71–91.
[36] Sun Y, Trevelyan J, Hattori G, Lu C. Discontinuous isogeometric boundary element (IGABEM) formulations in 3D automotive acoustics. Eng. Anal. Boundary Elem. 2019;105:303–11.
[37] Telles J, Oliveira R. Third degree polynomial transformation for boundary element integrals: Further improvements. Eng. Anal. Boundary Elem. 1994;13:135–41.
[38] Bishop RED, Price WG, Wu Y. A general linear hydroelasticity theory of floating structures moving in a seaway. Philosophical Transactions of the Royal Society of London. Series A, Mathematical and Physical Sciences 1986;316:375–426.
[39] Maestre J, Cuesta I, Pallares J. An unsteady 3d isogeometrical boundary element analysis applied to nonlinear gravity waves. Comput. Methods Appl. Mech. Eng. 2016;310:112–33.
[40] Abbasnia A, Guedes Soares C. Fully nonlinear propagation of waves in a uniform current using nurbs numerical wave tank. Ocean Eng. 2018;163:115–25.
[41] Junger MC, Feit D. Sound, structures and their interaction. Cambridge, Massachusetts: The MIT Press; 1972.
[42] L.E. Gilroy, Finite element calculations of cylinder natural frequencies, Technical Report, Defence Research Establishment Atlantic, 1993.
[43] Randall RJ. Fluid-structure interaction of submerged shells Ph.D. thesis. Department of Mechanical Engineering, Brunel University; 1990.
[44] Duffey TA, Pepin JE, Robertson AN, Steinzig ML, Coleman K. Vibrations of Complete Spherical Shells With Imperfections. J. Vib. Acoust. 2007;129:363–70.
[45] Peters H, Kessissoglou N, Marburg S. Modal decomposition of exterior acoustic-structure interaction. The Journal of the Acoustical Society of America 2013;133:2668–77.
[46] Piegl L, Tiller W. Surface approximation to scanned data. The Visual Computer 2000;16:386–95.